Estimating Floodplain Vegetative Roughness using Drone-Based Laser Scanning and Structure from Motion Photogrammetry

Charles Albert Aquilina

Thesis submitted to the faculty of the Virginia Polytechnic Institute and State University in partial fulfillment of the requirements for the degree of

Master of Science In

Biological Systems Engineering

W. Cully Hession, Chair

Jonathan A. Czuba

Thomas J. Pingel

July 23rd, 2020

Blacksburg, VA

Keywords: Drone Remote Sensing, Lidar, Structure from Motion Photogrammetry, Hydrodynamic Modeling, Manning's Roughness.

Estimating Floodplain Vegetative Roughness using Drone-Based Laser Scanning and Structure from Motion Photogrammetry

Charles A. Aquilina

Abstract

We compared high-resolution drone laser scanning (DLS) and structure from motion (SfM) photogrammetry-derived vegetation heights at the Virginia Tech StREAM Lab to determine Manning's roughness coefficient. We utilized two calibrated approaches and a calculated approach to estimate roughness from the two data sets (DLS & SfM), then utilized them in a two-dimensional (2D) hydrodynamic model (HEC-RAS). The calculated approach used plant characteristics to determine vegetative roughness, while the calibrated approaches involved adjusting roughness values until model outputs approached values of field data (e.g., velocity probe and visual observations). We compared the model simulations to seven actual high-flow events during the fall of 2018 and 2019 using measured field data (velocity sensors, groundwater well height, marked flood extents). We used a t-test to find that all models were not significantly different to water surface elevations from our 18 wells in the floodplain ($p > 0.05$). There was a decrease in RMSE (-0.02 m) using the calculated compared to the calibrated models. Another decrease in RMSE was found for DLS compared to SfM (-0.01 m). This increase might not justify the increased cost of a DLS setup over SfM (~$150,000 versus ~$2,000), though future studies are needed. Our results inform hydrodynamic modeling efforts, which are becoming increasingly important for management and planning as we experience increasing high-flow events in the eastern United States due to climate change.

Estimating Floodplain Vegetative Roughness using Drone-Based Laser Scanning and Structure from Motion Photogrammetry

Charles A Aquilina

General Audience Abstract

We compared high-resolution drone laser scanning (DLS) and structure from motion (SfM) photogrammetry-derived vegetation heights at the Virginia Tech StREAM Lab to improve flood modeling. DLS uses laser pulses to measure distances to create a three-dimensional (3D) point cloud of the landscape. SfM combines overlapping aerial images to create a 3D point cloud. Each method has limitations, such as cost (DLS) and accuracy (SfM). These remote sensing methods have been increasingly used to provide inputs to flood models, due to lower cost, and increased accuracy compared to airplane or satellite-based surveys. Quantifying roughness or resistance to flow can be extremely difficult and results in flood model accuracy problems. We used two forms of a calibrated approach, and a calculated approach to estimate roughness from the two data sets (DLS and SfM) which were then used in a two-dimensional (2D) flood model. We compared the model results to measured field data from seven actual high-flow events in Fall 2018 and 2019. We used statistics to determine compare the various techniques. We found that model results were not significantly different from measured water-surface elevations measured in the floodplain during floods. We also used root mean square error (RMSE) to measure the differences between modeled and observed data. There was slight decrease (-0.02 m) in error when comparing model results using the calculated and calibrated techniques. The error also decreased (-0.01 m) for simulations using the DLS versus SfM data sets. The improved accuracy due to the use of DLS might not be justified based on the increased cost of a DLS setup to SfM (~$150,000 versus ~$2,000), though future studies are needed. Insights from this analysis will help improve flood modeling, particularly as we plan for increasing high-flow events in the eastern Unites States due to climate change.

Acknowledgements

I would like to thank my parents, **Charles** and **Kathy Aquilina**, for their incredible support over the years. Your love and willingness to help me through some challenges gave me the base I needed to thrive.

Cully Hession has been a wonderful and fun mentor. Thank you for taking a chance on a kid without an engineering background.

Jonathan Czuba, thank you for helping with all the challenges I had with HEC-RAS, and being able to interpret the results of the model in a way I could easily understand.

Thomas Pingel, thanks for inviting me to your lab group meetings, and being the go-to person for lidar and structure from motion help.

Thank you to the Biological Systems Engineering department for funding my education and giving me teaching assistant opportunities. **Laura Lehmann**, thanks for teaching me all about drones, surveying and everything in between. Thanks also go out to **Jonathan Resop** (University of Maryland) for early help with understanding how to analyze lidar data. **Thomas Schubert** thanks for accepting my calls for surveying help even though you were already graduated. **Alexa Reed**, thank you for all your help diligently getting data, and dealing with me on long hot summer days getting well readings. **Beth Prior**, thanks for being a willing helper, always ready to edit my writing, or to go out and trudge through some very tall grass to survey flags. I'll miss hiking with you. Thanks to the rest of the Cully Clan, **Lauren Wind** and **Qualla Ketchum,** for always being a great sounding board, and making meetings fun. And to **Michelle Kott** for keeping me sane and making the most out of life during this coronavirus pandemic.

List of Abbreviations

2D	Two Dimensional
3D	Three Dimensional
ALS	Aerial Laser Scanning
CHM	Canopy Height Model
DEM	Digital Elevation Model
DLS	Drone Laser Scanning
DSM	Digital Surface Model
FEMA	Federal Emergency Management Agency
GCP	Ground Control Points
HEC-RAS	Hydrologic Engineering Center's River Analysis System
LAS	Log ASCII Standard
lidar	light detection and ranging
RMSE	Root Mean Square Error
SfM	Structure from Motion (photogrammetry)
UAV	Unoccupied Aerial Vehicle
USACE	United States Army Corps of Engineers
USGS	United States Geological Survey
m	meters
n	Manning's roughness coefficient
r^2	Coefficient of determination
RTK	Real Time Kinematic
StREAM Lab	Stream Research Education and Management Lab
UTM	Universal Transverse Mercator
WSE	Water Surface Elevation

Table of Contents

List of Figures

List of Tables

1. BACKGROUND

1.1 Introduction

Riverscapes are dynamic systems that are characterized by high connectivity and spatial complexity [1]. They provide a crucial societal and economic role, yet they also provide a significant danger to society in the form of flooding [2]. Due to climate change, the Eastern United States has experienced increased precipitation, which has led to more high-flow events in streams and rivers [3]. Modeling flooding will be of the utmost importance to prepare and plan for climate change impacts [4]. To do this, much research has been directed to two-dimensional (2D) hydrodynamic models, which are becoming the standard for flood modeling [5].

A major impediment to accurately modeling floods is Manning's roughness coefficient, *n*, which represents the resistance of flow in both channels and floodplains [6]. In the past, *n* has been determined by simple descriptions [7], comparison to images of streams and rivers [8], and by assignment based on landcover classes [9]. Another method, developed by Cowen [10], distributes total roughness amongst important components: particle size, surface irregularities, shape and size of the channel cross-section, obstructions, vegetation, and meandering. These tend to give very static roughness values throughout the floodplain [5]. Selected n values are typically then calibrated to match observed data, usually from USGS gages. These calibrated values are not based on physical characteristics, therefore the results of hydrodynamic models achieved using these *n* values should be met with skepticism [5].

Utilizing vegetative roughness equations based on flume studies [11–13] and field observations [14,15] provide better roughness estimates. Characteristics such as

vegetative density, stiffness, and vegetation height are utilized in these equations to estimate roughness [16]. The resulting datasets create spatially variable roughness values, taking into account variability of vegetation within the riverscape [5]. However, these formulas can require intensive field surveys, which are costly and time consuming. Fortunately, modified formulas have been created to take advantage of high-quality remotely sensed data to estimate roughness coefficients [5,17,18].

Remote sensing produces increasingly high-quality datasets in less time than traditional surveying [5,17–19]. Remote sensing has been mostly dominated by aerial surveys which utilize planes for heavy sensors such as light detecting and ranging, or lidar. However, recent advancements in technology and policy has expanded the use of unoccupied aerial vehicles (UAVs) or drones to conduct surveys in small to medium-sized study areas (<10 km^2) [20,21]. Many drone surveys utilize structure from motion (SfM) photogrammetry, which utilizes overlaps captured to create a point cloud of the landscape [19,22–25]. However, other sensors are now small and light enough to fit on drones, most notability lidar, which utilize laser pulses to create point clouds [20,21,26–28]. Lidar payloads on drones remain cost prohibitive for many people, and are not widespread [20]. Lidar can penetrate vegetation, meaning it can record ground points even in vegetated areas. This means that it has increased accuracy determining ground heights, and vegetation heights. Regardless, both SfM and drone laser scanning (DLS), combines the operational flexibility of drones with the high-resolution data to create accurate point clouds [21].

Given the need to accurately predict flooding, there is a need to assess and improve on studies utilizing UAVs for hydrodynamic applications. Limited studies have

compared SfM to DLS in mostly vegetative and topographic context [21,26]. Applying DLS and SfM data to hydrodynamic modeling is in its nascent stages [20,29,30]. Using the high-resolution data determined by UAV surveys will result in improved hydrodynamic modeling [30]. Improving 2D hydrodynamic modeling will make water resource projects, such as stream restorations, more accurate and potentially more resilient to the impacts of climate change [4,31]. Better hydrodynamic modeling will result in better restoration designs, as well as improved planning and management for flood impacts.

1.2 Research Goals and Objectives

The overarching goal of this study was to utilize UAV-based remote sensing to estimate roughness metrics in a riverscape environment. By using UAV data to improve parameter inputs to 2D hydrodynamic models, there is an expectation that model simulations will improve as well. An increase in the spatial variability of model parameters from traditional techniques to newly developed methods should further improve model accuracy and reduce uncertainty. A similar comparison will be made comparing models developed by DLS and SfM datasets. While DLS creates more accurate outputs, there is an expectation that high-resolution SfM data can be used to adequately predict floods as well. Predicting floods accurately is of the utmost importance as climate change has influenced hydrological cycles, resulting in increased frequency of high-flow events [3]. In summary, the specific objectives of this research were:

1. Evaluate 2D hydrodynamic model simulations of floods using roughness estimated based on DLS-based point clouds.
2. Evaluate 2D hydrodynamic model simulations of floods using roughness estimated based on SfM-based point clouds.
3. Compare 2D hydrodynamic modeling simulations using DLS-based versus SfM-based roughness estimates.

1.3 Organization of Thesis

The first chapter provides a background and justification for the research as well as a literature review that provides an overview of riverscapes, Manning's roughness, hydrodynamic modeling, and DLS and SfM photogrammetry. The second chapter a journal article that will be formatted to be submitted in a journal.

1.4 Literature Review

1.4.1 Introduction

As climate change results in increased high-flow events, simulating the impacts of flooding using hydrodynamic models has become essential [5]. The use of UAV derived high-quality datasets is being increasingly used for flood modeling [30,32]. There is a need to assess the various choices made when utilizing UAVs for hydrodynamic applications. This review of literature will focus on riverscapes, UAVs, DLS, SfM photogrammetry, and 2D hydrodynamic modeling to fulfill this need. This will unlock insights to topics such as the development of UAV flight parameters, best practices for point cloud classification and product creation, development of roughness rasters, and 2D hydrodynamic modeling practices, as well as setting the context for justifying the research efforts to follow.

1.4.2 Riverscapes

The earliest mention of the term "riverscape" was in 1968, when Leopold developed the term to explain the physical, biological, and aesthetic nature of rivers [33]. Fausch et al. [34] tweaked the term to encompass the energy, matter, and habitat structure of rivers. Riverscapes are complex mosaics of habitats characterized by high connectivity and spatial complexity [1]. Because riverscapes are dynamic systems that change in both space and time, it is a challenge for researchers to effectively study them [34]. In the past, spatial and temporal scales that drive riverscape ecosystem processes are often ignored by traditional sampling methodologies [34]. To solve this spatial and temporal issue, researchers have turned to remote sensing, which can provide measurements of

riverscape characteristics at a level comparable to field measurements in less time intensive and more continuous way [35].

Traditional monitoring of streams are conducted in small areas with high-resolution point samples, or in large areas with widely-spaced measurements that determine averages at watershed scales [36]. These methods were created due to the belief in the River Continuum Concept, which theorizes that river changes in a consistent and predictable way [37]. Instead, a "riverscape" approach has been used to explain the high amounts of spatial and temporal diversity, or the changes in the ecosystem in space and time, seen in streams and rivers [19]. Using a riverscape approach provides a more variable and continuous view of streams toward providing a better understanding of the processes and features that set the context for stream habitat [35]. The development of high-quality remotely-sensed topographic surveys, resulting in Digital Elevation Models (DEMs) of riverscapes, has been designated as a priority to achieve a more continuous view while capturing spatial and temporal variability of the riverscape [38].

1.4.3 Importance of River Measurements

Measurements of physical habitat parameters, such as substrate size, sinuosity, and channel slope, are used to quantify habitat characteristics of riverscapes [19]. Stream measurements are used for many applications, including stream restoration [39], flood routing [40], and sediment load estimation [41]. While money is increasingly being spent on ecological restoration, methods for quantifying project success are in their infancy [42]. Monitoring and assessing small to medium-scale stream restoration projects are often not adequate. For example, only 6% projects in the Chesapeake Bay watershed in the U.S. indicated that post-restoration monitoring occurred [39]. Without monitoring

information, it is hard to justify the effectiveness of a successful restoration project, or to learn lessons from projects that fail [43].

Measuring the spatial and temporal variation in physical parameters can be dynamically linked to habitat quality and distribution throughout the riverscape [30,44]. Remote sensing has long played an important role in measuring physical parameters of riverscapes as remote sensing encompasses a variety of relatively quick, cost-effective methods to collect a large extent of data [35,45]. Advances in structure-from-motion (SfM) photogrammetry and light detection and ranging (lidar) create high-quality point clouds that have been used in many biological and hydrological studies [46,47]. Common point cloud and spatial software such as ArcGIS Pro (ESRI, Redlands, CA) and LAStools (RapidLasso GmbH, Gichling, Germany) can be used to process point clouds to create Digital Elevation Models (DEM), and other products. Elevation models are commonly used to determine river measurements such as width, depth, gradient, and sinuosity, which can provide insights into stream ecosystems [48]. While much of the literature has utilized airplanes [49,50] and helicopters [36] to conduct photogrammetry and laser scans, For these reasons, UAVs are being increasingly used to monitor and measure riverscapes [30,51].

1.4.4 Unmanned Aerial Vehicles (UAV)

Military use has spurred the development of UAVs in the past 20 years, and recent advances have made them inexpensive enough for widespread civilian use [52]. Longer flight durations, improved safety, and decreased cost have made UAVs a common tool for research [53]. UAVs can be utilized to map areas at temporal and spatial scales that are unavailable for other remote sensing platforms and provide high

operational flexibility in terms of cost, time, and repeatability [54]. UAVs are increasingly utilized in civilian fields such as agriculture [55], archeology [56], and delivery systems [57]. UAV flights can be prepared and deployed quickly, in comparison to aerial (airplanes and helicopter) remote sensing, where third parties are often needed [20]. Due to the relative ease of conducting flights and the high-resolution datasets UAVs provide, researchers are increasingly turning to UAV systems to assess the hydrology, ecology, and geomorphology of riverscapes [19,35].

Increased incidents involving UAVs and other aircraft have called for regulation of UAV use [54,58,59]. In 2016, the United States of America (USA) Federal Aviation Administration (FAA), created the Part 107 rules for UAVs under 55 pounds. Rules include maintaining line of sight with drones at all times during a flight and keeping drones out of certain airspace. Many software packages will restrict UAVs from exceeding Part 107 legal flight altitudes (e.g., 120 m) and entering restricted airspace (e.g., airports, 8 km from Washington, D.C.) [59]. Commercial or research UAV operators must first obtain a UAV license from the FAA, which requires passing a multiple-choice test on Part 107 rules and regulations, registering the UAV with the FAA, and marking the UAV with the registration number [58,60]. The test focuses on topics that UAV users should be aware of, such as reading airspace maps, understanding airport weather reports, and UAV maintenance [60]. This is designed to keep pilots accountable for incidents and have knowledge of aircraft procedures and regulations [58].

A UAV system is typically paired with one or more sensors (or payloads), a ground control station, and a phone or laptop with flight control software [19]. Most UAVs used are either fixed wing, single, or multi-rotor, researchers have also turned to

blimps and kites, depending on the coverage needed and access to a suitable take off/landing areas [61,62]. Each platform has their own advantages and tradeoffs. Multirotor UAVs are more stable, ensuring better accuracy, but require multiple flights for larger areas [26]. Additionally, they can take larger payloads, meaning that multiple sensors can be used concurrently during a single flight [26]. Fixed-wing UAVs can fly longer distances, meaning they are the ideal choice for large study areas, but FAA regulations require continuous visual monitoring, meaning more people might be needed for the mission as visual observers and require large takeoff and landing spots [26]. Single rotor UAVs have also been used for data acquisition, and have intermediate operating range and stability compared to previously mentioned alternatives [20,21].

A UAV flight mission includes reconnaissance of the site, pre-flight field work, and the actual flight [63]. Reconnaissance includes a visual assessment of the site to check for hazards such as power lines and determining take off/landing areas. Before a flight, a flight plan must be created to set drone altitude, speed, and spacing of flight lines by creating way points. Pre-flight field work includes setting up the ground station that controls the drone, a quick check and maintenance of the drone, and for photogrammetry and setting up Ground Control Points (GCPs) [63]. During the flight, guidelines require maintaining line of sight on the UAV, either by the pilot or a visual observer that can communicate with the pilot, so the pilot is aware of potential hazards such as trees, power lines, planes, and birds [46].

Simple true-color red green blue (RGB) cameras are commonly utilized on drones, where the images can be post-processed using SfM photogrammetry techniques [64,65]. However, more sophisticated sensors are now small and light enough to mount

on UAVs, including lidar, thermal, and multispectral sensors [61]. The potential for UAVs to have complementary sensors, such as lidar and RGB cameras, will unlock unique insights of ecological processes during a single flight [26,62]. The availability of high-quality sensors coupled with the flexibility of UAVs make these tools ideal for river research and monitoring [30].

1.4.5 Structure-from-Motion (SfM) Photogrammetry

SfM techniques are commonly used in riverscape studies due to the inexpensive equipment needed to conduct UAV missions [19]. SfM photogrammetry utilizes overlapping photos from digital cameras to create a 3D point cloud of the landscape [46]. These techniques retain the high-quality imagery, which can be used for visual classification of features in the dataset, as well as the development of orthophotos, digital surface models (DSM) and 3D point clouds[62]. SfM approaches have been utilized for environmental monitoring projects, including: estimating tree height and biomass in forest inventory surveys [65]; mapping vegetation distribution [66]; monitoring coastlines [67]; quantifying presence and distribution of large woody debris [63]; monitoring of a stream restoration projects [43]; and tracking streambank retreat [29].

SfM requires more post processing for accurate 3D point clouds than lidar alternatives. The workflow required for SfM includes image preparation, image matching, inclusion of GCPs, building a dense point cloud, and outputting in LAS format (a common format for storing point clouds), exporting a DEM, and assessing accuracy [64,68]. Image preparation includes geotagging photos, or defining GPS coordinates for corresponding photos, as well as removing poor-quality images [63,68]. These GPS coordinates are typically determined by the UAV itself using an internal navigation

system (INS), or internal measurement unit (IMU) [29]. Commercial SfM software, such as Pix4Dmapper Pro (Pix4D, Lausanne, Switzerland) and Agisoft Metashape (Agisoft LLC, St. Petersburg, Russia), stitch aerial images together by finding common features to create 3D point clouds [47]. Additionally, there are publicly available packages, such as Ecosynth [65], which can be utilized to estimate forest biomass and canopy heights from SfM, and VisualSfM, which is a free alternative to creating point clouds [25].

GCPs are GPS-measured targets that have been placed in the study area to improve locational accuracy of the point cloud [67,69]. This process utilizes at least 3 GCPs to transform the model to an absolute coordinate system, which can then be compared with other georeferenced data, such as lidar datasets [70,71]. Agisoft Metashape, recommends using 10 GCPs, and these points cannot be in lines or regular patterns [63]. In lieu of GCPs, use of a survey grade, real time kinematic (RTK) receiver onboard the UAV improves accuracy compared to lower-end GPS units. However GCPs are recommended if the highest available accuracy is desired [72].

Other ways to improve accuracy of SfM products is to keep camera parameters consistent are using a high-quality camera, having a large amount of pictures with high overlaps, and utilizing slightly off vertical convergent imagery [25]. Creating the most accurate SfM models requires imagery taken from a variety of flight angles and altitudes [22,23,73]. Klien Hentz et al. [74] used SfM to compare physical habitat assessments done in the field. They evaluated wetted width, bankfull width, and distance to water and found that flying a UAV at 61 m gave the most accurate overall results, when compared to 30.5 m, 91.5 m and 122.0 m flight altitudes. However, many researchers recommend flying at lower altitude for producing high-resolution point clouds from SfM [69,75].

Many factors are important for accuracy and quality of SfM point clouds. Thus, planning the right criteria is important for providing useful data sets for determining physical parameters in the environment.

SfM has been used effectively to determine physical parameters in riverscapes. One possible use of SfM is to visually inspect high flood marks in the images in a post flood survey [76]. Dietrich [36] used SfM techniques to explore the relationship between channel width to slope and valley width to compare restored versus unrestored sections of a stream. SfM can also be used to detect geomorphic change in the riverscape and assess the spatial variability of erosion and aggradation [24]. SfM techniques have also been utilized to map geomorphological features of the riverscape and classified parameters such as grain size, width, and velocity [19].

SfM point clouds must be corrected to get accurate bathymetry metrics. Using optical data, bathymetry can be determined using correlations between water depth and water color, which works well for streams with low depths and turbidity [38]. Since this workflow uses photogrammetry, workflows utilizing both SfM and optical techniques are effective [77]. Woodget et al. [78] used a refraction correction in SfM directly to estimate water depths, which improved results in submerged areas with high error. Dietrich [79] developed a custom Python script to apply a refraction correction, which requires a UAV flight flown with off nadir camera angles at a time that minimizes glare and shadows. However, these optical methods only work in streams with clear water, other methods would need to be utilized in streams with high turbidity [79]. Despite the limitations, optical methods remain a good choice to pair with SfM, as it is relatively easy way to determine bathymetry.

Stitching together overlapping photos is computationally demanding and long processing times can be expected [70]. One study took a working day to process 134 non-geotagged images, using an i7 processor and 32 gigabytes of RAM [19]. This is because multiple images from angles are required to reduce error, as well as high overlaps (>80%) in order to make an accurate model [36,70,73]. Possible solutions to reduce processing times include utilizing geotagged images, new processing routings [80], and using point cloud management software such as CloudCompare (https://www.danielgm.net/cc/) to manage large datasets [19]. Cloud-based computing solutions, such as DroneDeploy (San Francisco, USA), can be used to preprocess data to shorten overall processing time [43].

Another limitation of SfM is that cameras do not penetrate through vegetation, meaning the ground points below the canopy will not be recorded, resulting in considerable error in DEM [63]. To rectify this, a convergent camera geometry has been proposed [36]. This method uses multiple camera angles with multiple flight altitudes, increasing the chance for the imagery to pick up ground points below the tree line [73]. The ToPCAT model [80] is a method to reduce noise in 3D point clouds. This model filters out vegetation in SFM point clouds to create more accurate DEMs and to create topographic statistics to determine physical parameters in a reach [80]. However, terrain filters are often arbitrary, and developed for Terrestrial Laser Scanning (TLS) or ALS data, and may not be applicable for aerial and drone lidar derived datasets. For example, the model cannot assess point scatter below the ground surface [76]. Due to the black-box nature of this and other models, verification that these models were designed for the types of data inputted is important to ensure accuracy [47]. Understanding the full SfM workflow ensures that the user can identify sources of error in the resulting products [25].

While vegetation limits the accuracy and, therefore effectiveness of SfM DEM generation, techniques exist for both the UAV mission and the post-processing workflow are available to minimize errors [36,80].

1.4.6 Laser Scanning

Laser scanning, or lidar, is a remote sensing method that measures distances to determine precise 3D information of the earth's surface characteristics, such as ground, vegetation, and manmade points [81]. Much of the literature relating to utilizing lidar to measure the natural environment is from forestry applications [30,82,83]. Lidar is the sensor of choice for change detection due to its ability to penetrate vegetation, which allows for the measurement of the underlying terrain [21]. Lidar has been increasingly utilized in other fields, including energy site selection [84], transportation [85], stormwater management [86], and flood mapping and modeling [87,88]. Additionally, lidar works well in tandem with other sensors, to create additional insights in ecological monitoring [18,26,62]. For example, lidar coupled with multispectral cameras has been utilized to effectively determine vegetative characteristics better than either sensor alone [26]. There is a growing interest in applying lidar techniques to hydrological and geomorphic properties of riverscapes, due to the high-quality topographic and vegetation data that are produced [20,38].

TLS is a ground-based lidar system. TLS can create very high density point clouds (>1000 points/m^2) due to its close proximity to the ground compared to other remote sensing techniques [41]. Researchers have used TLS to monitor flash floods [89], determine bed morphology [80], measure streambank retreat [41] and create habitat maps [90]. However, the dense point clouds create massive files, which need specialized tools

to extract useful products [80]. In addition, TLS surveys can be time intensive, and limited in extent, as the TLS system has to be set up manually [41]. Instead of manual setup it is possible to place TLS systems on vehicles to get data dynamically or in stop-go mode [38]. TLS is versatile, and can be put on a variety of vehicles, such as a tractor to monitor crops [91], trucks to analyze roads [92], boats to conduct a river survey [93], and amphibious vehicles to determine river and floodplain geometry [38]. TLS remain a useful survey method to get high resolution data in linear areas.

Aerial Laser Scanning (ALS) involves the use of lidar mounted on airplanes, which can be effective for mapping large areas, such as river watersheds [48]. Like SfM, ALS has been commonly used for forest inventory metrics, such as mean height, point density, and diameter of trees [94]. Researchers have also used ALS to assess riparian ecosystems. One study utilized ALS to determine physical parameters and other stream properties to map stream order, width, gradient, sinuosity, and solar shading [48]. This research determined that ALS had the capacity to estimate those parameters, but not to estimate water quality, bank stability, and tree species. Because national ALS datasets are increasingly available in western nations, researchers have been developing methods to utilized theses datasets to monitor large river systems [95,96]. These methods provide a way to continuously monitor the river channel network and characterize the hydromorphological status of river systems [95,96].

UAV or drone-based laser scanning (DLS) is a new method of remote sensing, due to the recent availability of lidar units that are light enough to be mounted on UAVs [51]. DLS are suitable for small (<1 km^2) to moderate (1-10 km^2) study areas, as they are cheaper and more operationally flexible than ALS flights [21]. DLS can provide high

resolution topographic data needed for geomorphological, hydrological modeling and change detection [26]. Since UAVs fly at lower altitudes than airplanes, the resolution of the point cloud outputs are higher; one study recorded 400 points/m^2 for DLS compared to 4.55 points/m^2 for a comparable ALS study [20]. DLS can produce points in hard-to-scan areas such as stream banks, and its high resolution means vegetation and small changes in the topography can be better assessed than ALS alternatives [48]. The increased resolution is important to measure parameters like channel width, low lying vegetation, and bed roughness.

DLS results create large point cloud datasets, which can be hard to classify and can require high-performance computing [20]. To avoid manual classification of these large datasets, researchers have turned to machine learning to classify data [62]. One family of machine learning techniques, supervised classification, uses training data to classify points in a way that reduces similarity between each classification [66]. LAStools (rapidlasso GmbH, Gilching, Germany), a commercial software package, can be utilized for point cloud dataset management, and also has algorithms for classification of point clouds [97]. The PDAL package in the python programming language (https://pdal.io/python.html), ArcGIS (ESRI, Redlands, California), and CloudCompare (https://www.danielgm.net/cc/), are other commonly used programming and software products for SfM and lidar projects [64,98].

Near infrared lidar is unable to pierce through water, because the water absorbs near infrared light, the bathymetry is not recorded in the point cloud [53,99]. Having accurate bathymetry, or the channel geometry below the water surface, is essential for hydrodynamic modeling [88]. There are lidar systems that employ green wavelengths that

can penetrate the water column to measure depths below the water surface to map bathymetry. This is commonly known as airborne bathymetric lidar, or green lidar [100]. While green lidar has been more commonly deployed on ALS systems, there are now bathymetric lidar units that have been developed for UAVs, but they are not widely available due to high cost [101].

To fully map riverscapes using near infrared lidar, the DLS data collection must be coupled with additional techniques to obtain bathymetry in the study area [88]. As a best management practice, researchers plan to fly at low-flow conditions to minimize the amount of channel geometry below the water surface [102]. While an optical correction can be applied to SfM, above-ground lidar does not create the true color imagery needed for this technique. Researchers normally couple lidar with other bathymetry techniques such as surveying cross sections using total stations [41], using multispectral sensors [53], or an Acoustic Doppler Current Profiler (ADCP) [103]. These bathymetry methods are used in tandem with above-ground near infrared lidar scans to get a holistic view of the topography of the riverscape. The resulting merged topographic data can give accurate ground points for a DEM, as well as a reference for vegetation metrics.

1.4.7 Comparison of DLS to SfM

Accuracy is of utmost concern for UAV studies, as SfM and DLS accuracy assessments are in its nascent stages [21]. To assess accuracy, many SfM DEMs use ALS DEMs as the reference [46,71,77]. There is considerable lack of accuracy in SfM-derived terrain models in highly vegetative areas, which limits efforts to track topographic change [65]. Correction methods taken from ALS procedures can create accurate SfM datasets. One study improved error to ±0.06 m using an onboard GPS unit with a 2.5 m positional

accuracy [23]. Another way to minimize error is the convergent camera orientation technique detailed in Dietrich [36], which helps minimize error by adding multiple camera angles. SfM techniques are the most accurate in areas that do not have obstructions, such as glaciers. Westoby et al. [70] found that 85.6 % of SfM point cloud data was within ± 0.5 m of TLS data. In a similar study, Draeyer and Strecha [71] compared SfM and ALS to assess the volume of rock stockpiles and found that the SfM overpredicted the ALS volume by 2% and 3% in two trials.

A standardized benchmark to assess horizontal and vertical accuracy is the American Society for Photogrammetry and Remote Sensing (ASPRS) Positional Accuracy Standards for Digital Geospatial Data [21]. Accuracy of UAV data is assessed by using the Root Mean Square Error (RMSE) in both the horizontal and vertical directions. In a SfM flight, Hugenholtz et al. [46] found a RSME of 29 cm in the z direction by comparing SfM to ALS lidar utilizing a fixed wing UAV. Tamminga et al. [30] used a quadcopter to improve the vertical RMSE to 8.8 cm in exposed areas without vegetation, and to 11.9 cm in areas submerged by water. Rusnak et al. [63] compared the accuracy of many studies and found the vertical RMSE ranged from 3.7 to 20 cm for ground points in exposed areas. Bathymetric elevations are also associated with error due to the uncertainty in optical methods mentioned earlier. In the same paper, bathymetric RSME ranged from 4.7 to 41 cm [63]. Other errors from SfM products include inaccurate GCP elevations, which make certain parts of the point cloud inaccurate [36,77]. Dietrich [36] also found errors due to parallel geometry of photos on flight lines.

DLS comparisons to other remote sensing systems is in its infancy [20]. One study compared DLS to ALS and SfM photogrammetry to assess different vegetated

terrains and found 2-3 times lower vertical error compared to ALS, and lower horizontal and vertical error compared to SfM [21]. The author was not able to make much of an interference between DLS and SfM photogrammetry due to differences in experimental design and suggested referencing the ASPRS standardized methodology for checkpoints quantity, spatial distribution, accuracy calculation and reporting. Another study compared field derived tree heights to heights determined by DLS and SfM [25]. They used a coefficient of determination, which is the proportion of the variance between the dependent and independent variables. They found a strong correlation for DLS ($r^2 = 0.9$), while SfM was less correlated, but still strong ($r^2 = 0.7$) [26]. SfM-derived grass heights have determined to not be strong, with one study reporting a RMSE of ± 1 m [22]. While drone based remote sensing is in its nascent stages, there is a standardized system and resulting literature to compare and improve data collection. This is especially important in SfM photogrammetry derived datasets, where vertical accuracy is a concern [64].

1.4.8 Manning's Roughness Coefficient

Roughness represents the resistance to flow in channels and floodplains [104]. It can influence numerous physical, chemical and biological processes including sediment transport, channel morphology, and aquatic habitat [105]. Roughness is the quality or state of having an uneven or irregular surface through various vegetative and topographic contributions [20]. Roughness is represented by Manning's roughness coefficient, *n*. This is an important variable in Manning's and Chezy's equations utilized in hydrology and hydrodynamic modeling [106,107]. This coefficient is ideally a total roughness measurement, that should take into consideration surface material, vegetation type, and

morphology [104]. Manning's *n* is one of the most sensitive parameters in hydrodynamic models, but often the hardest to measure [6].

Historically, roughness values were only estimated at certain points using visual observations [8] or simple calculations [104]. Chow [7] developed a lookup table to define roughness using simple descriptions or photographs of example streams in 1959, which remains the standard technique to this day. Chow's method has been applied using landcover units, such as the National Landcover Dataset, or NLCD, as a simple way to calibrate hydrodynamic models [9]. This assumption that only a few roughness measurements are needed for the entire system is a result of the belief that roughness values change predictively and gradually over the riverescape [35]. Since roughness metrics change over space and time, researchers have turned to other ways to determine roughness. Researchers have utilized satellite imagery [45], multispectral cameras [18], and tree-rings [108] to determine roughness in a more spatially variable way. Using UAV-based SfM and DLS derived high-resolution topography and vegetation data, better estimates of spatially variable roughness can be determined [20].

1.4.9 Vegetative Roughness

For most floodplains, the most important contribution to roughness is vegetation. Vegetation converts mean kinetic energy to turbulent kinetic energy in the channel, which affects drag and turbulence [109]. A study using traditional methods found that the mere presence of vegetation increased the roughness parameter by 500% [10]. Abu Aly et al. [5] found that adding spatially distributed vegetation roughness metrics in a 2D model resulted in a significant decrease in mean velocity (17.5%), and an increase in wetted area and mean depth in a channel (8%).

Traditionally, vegetation and large woody debris have been removed to reduce flooding risk [110]. Current management tends to encourage vegetation growth to increase streambank stabilization for stream restoration and other conservation projects, as vegetation can provide habitat, stabilize stream banks, and improve water quality by intercepting nutrients in the stream channel [39,111]. Studies to determine vegetative roughness in floodplains has been considered an important, yet challenging aspect of floodplain management [5,50].

Vegetation roughness is dependent on vegetation structure, which can be determined by canopy height, stem diameter, vegetation density, and presence of leaves [18]. Plant flexibility is an important variable in vegetative roughness, during a flood event, their leaves and branches are more likely to be underwater, impacting flow [112]. Rigid vegetation's contribution to roughness is dependent on flow depth, while flexible vegetation is affected more by velocity [107]. Some factors or characteristics can be extracted from remote sensing data for use in ecological and hydraulic modeling [5]. This is an important characteristic that needs attention in future studies.

Researchers have used vegetative attributes estimated from remotely sensed data to estimate roughness [16,18]. Many formulas have been developed using theoretical and empirical methods to determine vegetation resistance [113]. Most take into consideration drag, height, and other vegetation metrics from different vegetation types [111]. Cruzen et al. [66] used machine learning techniques to determine vegetation type and distribution using SfM, which could be used to differentiate between herbaceous and woody low vegetation. A technique was developed to utilize SfM data with a relationship of greenness of pixels to predict non-woody vegetation height [64]. After post-processing

the DLS or SfM point cloud, vegetation points can be used to extract relevant variables, such as vegetation density, and canopy height [65]. These vegetation metrics could then be used to determine vegetation roughness metrics.

Seasonal changes affect the amount of roughness due to vegetative changes throughout the year [104]. In fact, during the growing season, Manning's *n* can increase by 300% [114]. While in the spring and summer, when in-channel vegetation is fully grown, stream depths increase and velocity decrease [105]. UAV remote sensing is a promising technique for determining seasonal changes in roughness, due to the flexibility of being able to conduct flights seasonally and the ability of lidar to pick up minute changes in vegetation and topography [20].

Using these insights, many equations have been developed using empirical and theoretical data to determine vegetative roughness [111,113]. Wang and Zhang [111] utilized vegetative metrics such as height, density, and drag, to evaluate eleven vegetative roughness computational methods into 1D Hydrological Engineering Center-River Analysis System (HEC-RAS), a commonly used software developed by the U.S. Army Corps of Engineers (USACE). They found that methods which model vegetation as a rigid cylinder are applicable to determine stage dependent roughness, which is a dynamic roughness at certain flood depths [111]. Straatsma [14] related lidar derived vegetation to field derived vegetation density to estimate roughness with encouraging results (r^2 = 0.66). Mason et al. [17] created a method using simplified versions of equations developed by Kouwen [12,13,110] to require only vegetation heights to determine stage-dependent Manning's roughness values. This method provides a clear way to determine roughness into two vegetative classes, grasses (less than 1 m) and medium to tall

vegetation (greater than 1 m) [17]. Abu-Aly et al. [5] adapted a method by Casas et al. [115] to determine stage dependent roughness by using a relationship between water depth and vegetation height from ALS data. They found that vegetation dramaticallychanges flow paths in the floodplain [5]. Another finding was a correlation between discharge and roughness [5]. These studies emphasize the importance of determining vegetative roughness in the floodplain in order to create more accurate hydrodynamic models.

1.4.10 Topographic Roughness

Variability in topography can also be a major contributor to overall roughness. Surface roughness is often most pronounced on banks, where contributions to topographic roughness are determined by flow, soil cohesion, and vegetation influences [116]. Because DLS creates high-density point clouds, there is potential to utilize DLS to determine topographic roughness on streambanks, as well as tracking small changes in the topography [20]. To determine roughness, the point cloud software CloudCompare (https://www.danielgm.net/cc/) has a topographic roughness tool that uses a least-square method to compute a roughness value for each point in a point cloud [98]. Other methods, including the standard deviation of elevation using a least-square method determines a roughness metric using ArcGIS software (ESRI Inc., Redlands, CA) [20]. Another topographic roughness indicator is the standard deviation of detrended elevations, which is commonly used in earth sciences [24]. Marteau et al. [24] used this metric to create a roughness map of an ephemeral channel using SfM photogrammetry. Topographic indicators are only just a piece of the puzzle to determine total roughness.

1.4.11 Total Roughness

Another method to determine roughness is a Random Forest technique. Random Forest is a form of machine learning that uses hybrid classification and regression trees to test randomly selected variables, to assess how effective each individual variable predicts the final result [117]. This technique can utilize the multitude of data created by a variety of remote sensing platforms in a variety of environmental applications [62]. Medeiros et al. [118] used a variety of data, such as landcover to determine Manning's n using random forest methods. Many different roughness indicators using SfM, lidar, and other forms of remote sensing can be utilized to develop a spatially-variable roughness raster which can then be used for hydrodynamic modeling, such as in 2D HEC-RAS [119]. Some roughness indicators using point cloud products are provided in Table 1.

Table 1. Example of roughness indicators from lidar from Resop et al. [20].

Terrain and Vegetation Roughness Metrics	
$\mathbf{Min}_{\mathbf{ground}}$	Minimum elevation of ground and unassigned points; digital terrain model (DTM)
$\mathbf{Max}_{\mathbf{vegetation}}$	Maximum height of vegetation points; canopy height model (CHM)
$\boldsymbol{\sigma}_{\mathbf{ground}}$	Standard deviation of height of ground and unassigned points; topographic roughness
$\boldsymbol{\sigma}_{\mathbf{low\text{-}veg}}$	Standard deviation of height of low vegetation points; veg roughness
$\boldsymbol{\sigma}_{\mathbf{high\text{-}veg}}$	Standard deviation of height of high vegetation points; veg roughness
$\mathbf{\%}_{\mathbf{vegetation}}$	Decimal percentage of vegetation points out of total points; veg roughness

1.4.12 2D Hydrodynamic Modeling

Hydrodynamic models are used to predict flood extent and depth [119]. There are many hydrodynamic models that have been utilized with remotely sensed data to provide

input parameters for predicting flooding, such as Telemack 2D [50], MIKEFLOOD [108], RIVER2D [30] and SRH-2D [5]. One of the most common models in the USA is HEC-RAS [111,120,121]. HEC-RAS has been used extensively to model and predict floods, and is actually utilized to create Federal Emergency Management Agency (FEMA) flood maps [120]. HEC-RAS is also used for other water resource projects such as flood maps [120], dam removal projects [122], and stream restoration projects [123]. The 2D HEC-RAS (USACE) performs unsteady flow routing using the Saint Venant equations using either 1D, 2D, or a combination of the two [124]. 2D models have increasingly been utilized, taking advantage of high-level topographic information from lidar, bathymetric surveys, and other data sources to model floods in waterways with increasing accuracy [5]. 2D models produce spatially varying outputs of water surface elevation, flood depths, and velocities at each computation point [5,50]. This is useful to compare to field data spread throughout the study area. Using 2D models, researchers have been able to compare an ALS derived roughness parameterization method with roughness derived from traditional methods [17,18,50].

The ability to estimate roughness at high resolutions and high quality will improve hydrodynamic modeling [6]. Roughness ideally should be specified for each computational cell or pixel, but difficulties in scale and experimental constraints have limited researchers to using simple methods to calibrate constant, approximate values of roughness [121]. Remotely sensed data can provide continuously varying roughness values in small 10 cm pixels in raster format [20]. A roughness raster file is often a direct input for 2D hydrodynamic modeling, which is emerging as a standard for hydraulic modeling of flood conditions [5]. Other important inputs in hydrodynamic models

include a DEM, slope, flow area, and upstream and downstream flow conditions [124]. Because both SfM and lidar do not adequately estimate bathymetry, methods mentioned previously must be utilized to obtain detailed underwater topography.

Researchers have utilized data from hydrodynamic modeling to compare to flood extents to many datasets. For example, Cobby et al. [50] used synthetic aperture radar (SAR) to determine flood extents to compare to model extents. Tamminga et al. [30] used field derived flood heights to compare to model flood heights. These data were then compared using a t-test [50], and RMSE [30] to determine effectiveness of the model. A t-test compares two sets of data to see how significantly alike or different they are [50]. Cobby et al. [50] used this technique to determine if the model was successful at predicting flood levels compared to the field data.

1.4.13 Summary

Riverscapes are complex, dynamic systems that change in both space and time. Remote sensing is in the infancy of being utilized to measure physical parameters of riverscapes, which can be directly linked to habitat quality and spatial distribution of hydrogeomorphology. SfM and lidar techniques are used to create 3D point clouds, which can be utilized by software packages such as LAStools and ArcGIS to manage and classify data. These georeferenced, classified point clouds can be used to create DEMs and vegetation models. Physical parameters such as channel width, gradient, bank stability, canopy cover, and other stream attributes related to hydrogeomorphic and ecological processes can be parsed from the data. Using vegetative metrics derived from 3D point cloud data, roughness estimations can then be made into a final, spatially varying roughness raster for providing continuous view of roughness in a riverscape

across both space and time. These detailed roughness data layers can then be used to develop improve 2D hydrodynamic modeling, thereby providing insight to how the riverscape responds to flooding and other impacts.

References

1. Allan, J.D. Landscapes and riverscapes: The influence of land use on stream ecosystems. *Annu. Rev. Ecol. Evol. Syst.* **2004**, *35*, 257–284, doi:10.1146/annurev.ecolsys.35.120202.110122.
2. Tomsett, C.; Leyland, J. Remote sensing of river corridors: A review of current trends and future directions. *River Res. Appl.* 2019, *35*, 779–803.
3. Groisman, P.Y.; Knight, R.W.; Karl, T.R. Heavy Precipitation and High Streamflow in the Contiguous United States: Trends in the Twentieth Century. *Bull. Am. Meteorol. Soc.* **2001**, *82*, 219–246, doi:10.1175/1520-0477(2001)082<0219:HPAHSI>2.3.CO;2.
4. Hirabayashi, Y.; Mahendran, R.; Koirala, S.; Konoshima, L.; Yamazaki, D.; Watanabe, S.; Kim, H.; Kanae, S. Global flood risk under climate change. *Nat. Clim. Chang.* **2013**, *3*, 816–821, doi:10.1038/nclimate1911.
5. Abu-Aly, T.R.; Pasternack, G.B.; Wyrick, J.R.; Barker, R.; Massa, D.; Johnson, T. Effects of LiDAR-derived, spatially distributed vegetation roughness on two-dimensional hydraulics in a gravel-cobble river at flows of 0.2 to 20 times bankfull. *Geomorphology* **2014**, *206*, 468–482, doi:10.1016/j.geomorph.2013.10.017.
6. Keys, T.A.; Jones, C.N.; Scott, D.T.; Chuquin, D. A cost-effective image processing approach for analyzing the ecohydrology of river corridors. *Limnol.*

Oceanogr. Methods **2016**, *14*, 359–369, doi:10.1002/lom3.10095.

7. Chow, V. *Open-Channel Hydraulics*; McGraw-Hill Book Company, Inc: New York, NY, USA, 1959; ISBN 978-0-07-010776-2.
8. Barnes, H. *Roughness characteristics of natural channels*; USGS Water Supply Paper, 1969; Vol. 7;.
9. Janssen, C. *Manning's n Values for Various Land Covers To Use for Dam Breach Analyses by NRCS in Kansas (See Recommendations and Cautions on Page 2)*; 2016;
10. Cowan, W.L. Estimating hydraulic roughness coefficients: Agricultural Engineering,. *Agric. Eng.* **1956**, *337*, 470–500.
11. Kouwen, N.N.; Li, R.-M. Biomechanics of vegetative channel linings. *J. Hydraul. Div.* **1980**, *106*.
12. Kouwen, N. Field estimation of the biomechanical properties of grass. *J. Hydraul. Res.* **1988**, *26*, 559–568, doi:10.1080/00221688809499193.
13. Fathi-Maghadam, M.; Kouwen, N. Nonrigid, nonsubmerged, vegetative roughness on floodplains. *J. Hydraul. Eng.* **1997**, *123*, 51–57, doi:10.1061/(ASCE)0733-9429(1997)123:1(51).
14. Straatsma, M.W. Quantitative mapping of hydrodynamic vegetation density of floodplain forests under leaf-off conditions using airborne laser scanning. *Photogramm. Eng. Remote Sensing* **2008**, *74*, 987–998, doi:10.14358/PERS.74.8.987.
15. Ardıçlıoğlu, M.; Kuriqi, A. Calibration of channel roughness in intermittent rivers using HEC-RAS model: case of Sarimsakli creek, Turkey. *SN Appl. Sci.* **2019**, *1*,

1080, doi:10.1007/s42452-019-1141-9.

16. Junna, W.; Zhonglong, Z. Evaluating Riparian Vegetation Roughness Computation Methods Integrated within HEC-RAS. *J. Hydraul. Eng.* **2019**, *145*, 4019020, doi:10.1061/(ASCE)HY.1943-7900.0001597.
17. Mason, D.C.; Cobby, D.M.; Horritt, M.S.; Bates, P.D. Floodplain friction parameterization in two-dimensional river flood models using vegetation heights derived from airborne scanning laser altimetry. *Hydrol. Process.* **2003**, *17*, 1711–1732, doi:10.1002/hyp.1270.
18. Straatsma, M.W.; Baptist, M.J. Floodplain roughness parameterization using airborne laser scanning and spectral remote sensing. *Remote Sens. Environ.* **2008**, *112*, 1062–1080, doi:10.1016/j.rse.2007.07.012.
19. Woodget, A.S.; Austrums, R.; Maddock, I.P.; Habit, E. Drones and digital photogrammetry: from classifications to continuums for monitoring river habitat and hydromorphology. *Wiley Interdiscip. Rev. Water* **2017**, *4*, e1222, doi:10.1002/wat2.1222.
20. Resop, J.P.; Lehmann, L.; Hession, W.C. Drone Laser Scanning for Modeling Riverscape Topography and Vegetation: Comparison with Traditional Aerial Lidar. *Drones* 2019, *3*, 35.
21. Kucharczyk, M.; Hugenholtz, C.H.; Zou, X. UAV–LiDAR accuracy in vegetated terrain. *J. Unmanned Veh. Syst.* **2018**, *6*, 212–234, doi:10.1139/juvs-2017-0030.
22. Thomas, A.F.; Frazier, A.E.; Mathews, A.J.; Cordova, C.E. Impacts of Abrupt Terrain Changes and Grass Cover on Vertical Accuracy of UAS-SfM Derived Elevation Models. *Pap. Appl. Geogr.* **2020**, 1–16,

doi:10.1080/23754931.2020.1782254.

23. Carbonneau, P.E.; Dietrich, J.T. Cost-effective non-metric photogrammetry from consumer-grade sUAS: implications for direct georeferencing of structure from motion photogrammetry. *Earth Surf. Process. Landforms* **2017**, *42*, 473–486, doi:10.1002/esp.4012.

24. Marteau, B.; Vericat, D.; Gibbins, C.; Batalla, R.J.; Green, D.R. Application of Structure-from-Motion photogrammetry to river restoration. *Earth Surf. Process. Landforms* **2017**, *42*, 503–515, doi:10.1002/esp.4086.

25. Smith, M.W.; Carrivick, J.L.; Quincey, D.J. Structure from motion photogrammetry in physical geography. *Prog. Phys. Geogr.* **2015**, *40*, 247–275, doi:10.1177/0309133315615805.

26. Sankey, T.; Donager, J.; McVay, J.; Sankey, J.B. UAV lidar and hyperspectral fusion for forest monitoring in the southwestern USA. *Remote Sens. Environ.* **2017**, *195*, 30–43, doi:10.1016/j.rse.2017.04.007.

27. Wallace, L.; Lucieer, A.; Watson, C.; Turner, D. Development of a UAV-LiDAR system with application to forest inventory. *Remote Sens.* 2012, *4*, 1519–1543.

28. Chisholm, R.A.; Cui, J.; Lum, S.K.Y.; Chen, B.M. UAV LiDAR for below-canopy forest surveys. *J. Unmanned Veh. Syst.* **2013**, *01*, 61–68, doi:10.1139/juvs-2013-0017.

29. Mirijovskỳ, J.; Langhammer, J. Multitemporal monitoring of the morphodynamics of a mid-mountain stream using UAS photogrammetry. *Remote Sens.* **2015**, *7*, 8586–8609, doi:10.3390/rs70708586.

30. Tamminga, A.; Hugenholtz, C.; Eaton, B.; Lapointe, M. Hyperspatial Remote

Sensing of Channel Reach Morphology and Hydraulic Fish Habitat Using an Unmanned Aerial Vehicle (UAV): A First Assessment in the Context of River Research and Management. *River Res. Appl.* **2015**, *31*, 379–391, doi:10.1002/rra.2743.

31. S., S.J. Use of a 2D Hydrodynamic Model for Stream Restoration Design of High-flow Habitat in Low-gradient Midwest Streams. *Prot. Restor. Urban Rural Streams* 2004, 242–251.
32. Langhammer, J.; Bernsteinová, J.; Miřijovský, J. Building a High-Precision 2D Hydrodynamic Flood Model Using UAV Photogrammetry and Sensor Network Monitoring. *Water* 2017, *9*.
33. Leopold, L.B.; O'Brien Marchand, M. On the Quantitative Inventory of the Riverscape. *Water Resour. Res.* **1968**, *4*, 709–717, doi:10.1029/WR004i004p00709.
34. Fausch, K.D.; Torgersen, C.E.; Baxter, C. V.; Li, H.W. Landscapes to Riverscapes: Bridging the Gap between Research and Conservation of Stream Fishes. *Bioscience* **2002**, *52*, 483, doi:10.1641/0006-3568(2002)052[0483:ltrbtg]2.0.co;2.
35. Carbonneau, P.; Fonstad, M.A.; Marcus, W.A.; Dugdale, S.J. Making riverscapes real. *Geomorphology* **2012**, *137*, 74–86, doi:10.1016/j.geomorph.2010.09.030.
36. Dietrich, J.T. Riverscape mapping with helicopter-based Structure-from-Motion photogrammetry. *Geomorphology* **2016**, *252*, 144–157, doi:10.1016/j.geomorph.2015.05.008.
37. Vannote, R.L.; Minshall, G.W.; Cummins, K.W.; Sedell, J.R.; Cushing, C.E. The

river continuum concept. *Can. J. Fish. Aquat. Sci.* **1980**, *37*, 130–137, doi:10.1139/f80-017.

38. Williams, R.D.; Brasington, J.; Vericat, D.; Hicks, D.M. Hyperscale terrain modelling of braided rivers: Fusing mobile terrestrial laser scanning and optical bathymetric mapping. *Earth Surf. Process. Landforms* **2014**, *39*, 167–183, doi:10.1002/esp.3437.

39. Bernhardt, E.S.; Palmer, M.A.; Allan, J.D.; Alexander, G.; Barnas, K.; Brooks, S.; Carr, J.; Clayton, S.; Dahm, C.; Follstad-Shah, J.; et al. Synthesizing U.S. river restoration efforts. *Science (80-.).* **2005**, *308*, 636–637, doi:10.1126/science.1109769.

40. Yang, Y.; Endreny, T.A.; Nowak, D.J. *Application of advection-diffusion routing model to flood wave propagation: A case study on Big Piney River, Missouri USA*; 2016; Vol. 27;.

41. Resop, J.P.; Hession, W.C. Terrestrial laser scanning for monitoring streambank retreat: Comparison with traditional surveying techniques. *J. Hydraul. Eng.* **2010**, *136*, 794–798, doi:10.1061/(ASCE)HY.1943-7900.0000233.

42. Palmer, M.A.; Hondula, K.L.; Koch, B.J. Ecological Restoration of Streams and Rivers: Shifting Strategies and Shifting Goals. *Annu. Rev. Ecol. Evol. Syst.* **2014**, *45*, 247–269, doi:10.1146/annurev-ecolsys-120213-091935.

43. Langhammer, J. UAV monitoring of stream restorations. *Hydrology* **2019**, *6*, doi:10.3390/hydrology6020029.

44. Maddock, I. The importance of physical habitat assessment for evaluating river health. *Freshw. Biol.* **1999**, *41*, 373–391, doi:10.1046/j.1365-2427.1999.00437.x.

45. Hugue, F.; Lapointe, M.; Eaton, B.C.; Lepoutre, A. Satellite-based remote sensing of running water habitats at large riverscape scales: Tools to analyze habitat heterogeneity for river ecosystem management. *Geomorphology* **2016**, *253*, 353–369, doi:10.1016/j.geomorph.2015.10.025.

46. Hugenholtz, C.H.; Whitehead, K.; Brown, O.W.; Barchyn, T.E.; Moorman, B.J.; LeClair, A.; Riddell, K.; Hamilton, T. Geomorphological mapping with a small unmanned aircraft system (sUAS): Feature detection and accuracy assessment of a photogrammetrically-derived digital terrain model. *Geomorphology* **2013**, *194*, 16–24, doi:10.1016/j.geomorph.2013.03.023.

47. Micheletti, N.; Chandler, J.H.; Lane, S.N. Structure from motion (SFM) photogrammetry. **2015**.

48. Tompalski, P.; Coops, N.C.; White, J.C.; Wulder, M.A.; Yuill, A. Characterizing streams and riparian areas with airborne laser scanning data. *Remote Sens. Environ.* **2017**, *192*, 73–86, doi:10.1016/j.rse.2017.01.038.

49. Pepe, M.; Fregonese, L.; Scaioni, M. Planning airborne photogrammetry and remote-sensing missions with modern platforms and sensors. *Eur. J. Remote Sens.* **2018**, *51*, 412–435, doi:10.1080/22797254.2018.1444945.

50. Cobby, D.M.; Mason, D.C.; Horritt, M.S.; Bates, P.D. Two-dimensional hydraulic flood modelling using a finite-element mesh decomposed according to vegetation and topographic features derived from airborne scanning laser altimetry. *Hydrol. Process.* **2003**, *17*, 1979–2000, doi:10.1002/hyp.1201.

51. Lin, Y.; Hyyppä, J.; Jaakkola, A. Mini-UAV-borne LIDAR for fine-scale mapping. *IEEE Geosci. Remote Sens. Lett.* **2011**, *8*, 426–430,

doi:10.1109/LGRS.2010.2079913.

52. Watts, A.C.; Ambrosia, V.G.; Hinkley, E.A. Unmanned aircraft systems in remote sensing and scientific research: Classification and considerations of use. *Remote Sens.* **2012**, *4*, 1671–1692, doi:10.3390/rs4061671.

53. Legleiter, C.J. Remote measurement of river morphology via fusion of LiDAR topography and spectrally based bathymetry. *Earth Surf. Process. Landforms* **2012**, *37*, 499–518, doi:10.1002/esp.2262.

54. Stöcker, C.; Bennett, R.; Nex, F.; Gerke, M.; Zevenbergen, J. Review of the current state of UAV regulations. *Remote Sens.* **2017**, *9*, doi:10.3390/rs9050459.

55. Reinecke, M.; Prinsloo, T. The influence of drone monitoring on crop health and harvest size. In Proceedings of the 2017 1st International Conference on Next Generation Computing Applications, NextComp 2017; 2017; pp. 5–10.

56. Campana, S. Drones in Archaeology. State-of-the-art and Future Perspectives. *Archaeol. Prospect.* **2017**, *24*, 275–296, doi:10.1002/arp.1569.

57. Sanjab, A.; Saad, W.; Basar, T. Prospect theory for enhanced cyber-physical security of drone delivery systems: A network interdiction game. In Proceedings of the IEEE International Conference on Communications; 2017; pp. 1–6.

58. Cracknell, A.P. UAVs: regulations and law enforcement. *Int. J. Remote Sens.* **2017**, *38*, 3054–3067, doi:10.1080/01431161.2017.1302115.

59. Gettinger, D.; Michel, A.H. Drone sightings and close encounters: An analysis. *Bard Coll. Cent. Study Drone* **2015**, 1–28.

60. Chiang, B. FAA Best Practices, State Laws, Local Rules, and Police Efforts: A Multi-Faceted Approach to Regulating Police UAVs in the US. *U. La Verne L.*

Rev. **2016**, *38*, 201.

61. DeBell, L.; Anderson, K.; Brazier, R.E.; King, N.; Jones, L. Water resource management at catchment scales using lightweight UAVs: current capabilities and future perspectives. *J. Unmanned Veh. Syst.* **2016**, *4*, 7–30, doi:10.1139/juvs-2015-0026.

62. Buters, T.M.; Bateman, P.W.; Robinson, T.; Belton, D.; Dixon, K.W.; Cross, A.T. Methodological ambiguity and inconsistency constrain unmanned aerial vehicles as a silver bullet for monitoring ecological restoration. *Remote Sens.* **2019**, *11*, doi:10.3390/rs11101180.

63. Rusnák, M.; Sládek, J.; Kidová, A.; Lehotský, M. Template for high-resolution river landscape mapping using UAV technology. *Meas. J. Int. Meas. Confed.* **2018**, *115*, 139–151, doi:10.1016/j.measurement.2017.10.023.

64. van Iersel, W.; Straatsma, M.; Addink, E.; Middelkoop, H. Monitoring height and greenness of non-woody floodplain vegetation with UAV time series. *ISPRS J. Photogramm. Remote Sens.* **2018**, *141*, 112–123, doi:10.1016/j.isprsjprs.2018.04.011.

65. Dandois, J.P.; Ellis, E.C. High spatial resolution three-dimensional mapping of vegetation spectral dynamics using computer vision. *Remote Sens. Environ.* **2013**, *136*, 259–276, doi:10.1016/j.rse.2013.04.005.

66. Cruzan, M.B.; Weinstein, B.G.; Grasty, M.R.; Kohrn, B.F.; Hendrickson, E.C.; Arredondo, T.M.; Thompson, P.G. Small Unmanned Aerial Vehicles (Micro-Uavs, Drones) in Plant Ecology. *Appl. Plant Sci.* **2016**, *4*, 1600041, doi:10.3732/apps.1600041.

67. Gonçalves, J.A.; Henriques, R. UAV photogrammetry for topographic monitoring of coastal areas. *ISPRS J. Photogramm. Remote Sens.* **2015**, *104*, 101–111, doi:10.1016/j.isprsjprs.2015.02.009.

68. Lucieer, A.; Jong, S.M. d.; Turner, D. Mapping landslide displacements using Structure from Motion (SfM) and image correlation of multi-temporal UAV photography. *Prog. Phys. Geogr.* **2014**, *38*, 97–116, doi:10.1177/0309133313515293.

69. Gauci, A.A.; Brodbeck, C.J.; Poncet, A.M.; Knappenberger, T. Assessing the geospatial accuracy of aerial imagery collected with various UAS platforms. *Trans. ASABE* **2018**, *61*, 1823–1829, doi:10.13031/trans.12852.

70. Westoby, M.J.; Brasington, J.; Glasser, N.F.; Hambrey, M.J.; Reynolds, J.M. "Structure-from-Motion" photogrammetry: A low-cost, effective tool for geoscience applications. *Geomorphology* **2012**, *179*, 300–314, doi:10.1016/j.geomorph.2012.08.021.

71. Draeyer, B.; Strecha, C. How accurate are UAV surveying methods? *Pix4D White Pap.* **2014**, 1–8.

72. Hugenholtz, C.; Brown, O.; Walker, J.; Barchyn, T.; Nesbit, P.; Kucharczyk, M.; Myshak, S. Spatial accuracy of UAV-derived orthoimagery and topography: Comparing photogrammetric models processed with direct geo-referencing and ground control points. *Geomatica* **2016**, *70*, 21–30, doi:10.5623/cig2016-102.

73. Fonstad, M.A.; Dietrich, J.T.; Courville, B.C.; Jensen, J.L.; Carbonneau, P.E. Topographic structure from motion: A new development in photogrammetric measurement. *Earth Surf. Process. Landforms* **2013**, *38*, 421–430,

doi:10.1002/esp.3366.

74. Klein Hentz, Â.; Kinder, P.; Hubbart, J.; Kellner, E. Accuracy and Optimal Altitude for Physical Habitat Assessment (PHA) of Stream Environments Using Unmanned Aerial Vehicles (UAV). *Drones* **2018**, *2*, 20, doi:10.3390/drones2020020.

75. Kameyama, S.; Sugiura, K. Estimating Tree Height and Volume Using Unmanned Aerial Vehicle Photography and SfM Technology, with Verification of Result Accuracy. *Drones* **2020**, *4*, 19.

76. Smith, M.W.; Carrivick, J.L.; Hooke, J.; Kirkby, M.J. Reconstructing flash flood magnitudes using "Structure-from-Motion": A rapid assessment tool. *J. Hydrol.* **2014**, *519*, 1914–1927, doi:10.1016/j.jhydrol.2014.09.078.

77. Javernick, L.; Brasington, J.; Caruso, B. Modeling the topography of shallow braided rivers using Structure-from-Motion photogrammetry. *Geomorphology* **2014**, *213*, 166–182, doi:10.1016/j.geomorph.2014.01.006.

78. Woodget, A.S.; Carbonneau, P.E.; Visser, F.; Maddock, I.P. Quantifying submerged fluvial topography using hyperspatial resolution UAS imagery and structure from motion photogrammetry. *Earth Surf. Process. Landforms* **2015**, *40*, 47–64, doi:10.1002/esp.3613.

79. Dietrich, J.T. Bathymetric Structure-from-Motion: extracting shallow stream bathymetry from multi-view stereo photogrammetry. *Earth Surf. Process. Landforms* 2017, *42*, 355–364.

80. Brasington, J.; Vericat, D.; Rychkov, I. Modeling river bed morphology, roughness, and surface sedimentology using high resolution terrestrial laser

scanning. *Water Resour. Res.* **2012**, *48*, doi:10.1029/2012WR012223.

81. NOAA What is LIDAR?

82. Tang, L.; Shao, G. Drone remote sensing for forestry research and practices. *J. For. Res.* **2015**, *26*, 791–797, doi:10.1007/s11676-015-0088-y.

83. Dubayah, R.O.; Drake, J.B. Lidar Remote Sensing for Forestry. *J. For.* **2000**, *98*, 44–52, doi:10.1093/jof/98.6.44.

84. Szabó, S.; Enyedi, P.; Horváth, M.; Kovács, Z.; Burai, P.; Csoknyai, T.; Szabó, G. Automated registration of potential locations for solar energy production with Light Detection and Ranging (LiDAR) and small format photogrammetry. *J. Clean. Prod.* **2016**, *112*, 3820–3829, doi:10.1016/j.jclepro.2015.07.117.

85. Williams, K.; Olsen, M.J.; Roe, G. V.; Glennie, C. Synthesis of transportation applications of mobile LIDAR. *Remote Sens.* 2013, *5*, 4652–4692.

86. James, M.B.; Dymond, R.L. Bioretention hydrologic performance in an urban stormwater network. *J. Hydrol. Eng.* **2012**, *17*, 431–436, doi:10.1061/(ASCE)HE.1943-5584.0000448.

87. Carolina, N.; Mapping, F. *LiDAR-Derived Flood-Inundation Maps for Real-Time Flood-Mapping Applications , Tar River Basin , North Carolina Scientific Investigations Report 2007 – 5032*; 2007;

88. Merwade, V.; Cook, A.; Coonrod, J. GIS techniques for creating river terrain models for hydrodynamic modeling and flood inundation mapping. *Environ. Model. Softw.* **2008**, *23*, 1300–1311, doi:10.1016/j.envsoft.2008.03.005.

89. Tamari, S.; Guerrero-Meza, V. Flash flood monitoring with an inclined Lidar installed at a river bank: Proof of concept. *Remote Sens.* **2016**, *8*,

doi:10.3390/rs8100834.

90. Milan, D.J.; Heritage, G.L.; Large, A.R.G.; Entwistle, N.S. Mapping hydraulic biotopes using terrestrial laser scan data of water surface properties. *Earth Surf. Process. Landforms* **2010**, *35*, 918–931, doi:10.1002/esp.1948.

91. Sun, S.; Li, C.; Paterson, A.H. In-field high-throughput phenotyping of cotton plant height using LiDAR. *Remote Sens.* **2017**, *9*, doi:10.3390/rs9040377.

92. El-Halawany, S.I.; Lichti, D.D. Detection of road poles from mobile terrestrial laser scanner point cloud. In Proceedings of the 2011 International Workshop on Multi-Platform/Multi-Sensor Remote Sensing and Mapping, M2RSM 2011; 2011; pp. 1–6.

93. Alho, P.; Kukko, A.; Hyyppä, H.; Kaartinen, H.; Hyyppä, J.; Jaakkola, A. Application of boat-based laser scanning for river survey. *Earth Surf. Process. Landforms* **2009**, *34*, 1831–1838, doi:10.1002/esp.1879.

94. Næsset, E. Area-Based Inventory in Norway – From Innovation to an Operational Reality. In *Forestry Applications of Airborne Laser Scanning: Concepts and Case Studies*; Maltamo, M., Næsset, E., Vauhkonen, J., Eds.; Springer Netherlands: Dordrecht, 2014; pp. 215–240 ISBN 978-94-017-8663-8.

95. Demarchi, L.; Bizzi, S.; Piégay, H. Hierarchical object-based mapping of riverscape units and in-stream mesohabitats using lidar and VHR imagery. *Remote Sens.* **2016**, *8*, doi:10.3390/rs8020097.

96. Rinaldi, M.; Belletti, B.; Bussettini, M.; Comiti, F.; Golfieri, B.; Lastoria, B.; Marchese, E.; Nardi, L.; Surian, N. New tools for the hydromorphological assessment and monitoring of European streams. *J. Environ. Manage.* **2017**, *202*,

363–378, doi:10.1016/j.jenvman.2016.11.036.

97. Isenburg, M. LAStools rapid software for LiDAR processing. **2014**, 57.

98. Woodget, A.S.; Austrums, R. Subaerial gravel size measurement using topographic data derived from a UAV-SfM approach. *Earth Surf. Process. Landforms* **2017**, *42*, 1434–1443, doi:10.1002/esp.4139.

99. Kinzel, P.J.; Legleiter, C.J.; Nelson, J.M. Mapping River Bathymetry With a Small Footprint Green LiDAR: Applications and Challenges1. *JAWRA J. Am. Water Resour. Assoc.* **2013**, *49*, 183–204, doi:10.1111/jawr.12008.

100. Hilldale, R.C.; Raff, D. Assessing the ability of airborne LiDAR to map river bathymetry. *Earth Surf. Process. Landforms* **2008**, *33*, 773–783, doi:10.1002/esp.1575.

101. Tapken, P. Bathymetric Lidar Sensors and UAVs.

102. Cavalli, M.; Tarolli, P.; Marchi, L.; Dalla Fontana, G. The effectiveness of airborne LiDAR data in the recognition of channel-bed morphology. *Catena* **2008**, *73*, 249–260, doi:10.1016/j.catena.2007.11.001.

103. Milan, D.J.; Heritage, G.L. LiDAR and ADCP Use in Gravel-Bed Rivers: Advances Since GBR6. In *Gravel-Bed Rivers: Processes, Tools, Environments*; John Wiley & Sons, Ltd, 2012; pp. 286–302 ISBN 9780470688908.

104. Arcement, G.J.; Schneider, V.R. *Guide for selecting Manning's roughness coefficients for natural channels and flood plains*; 1989; Vol. 2339;.

105. Curran, J.C.; Hession, W.C. Vegetative impacts on hydraulics and sediment processes across the fluvial system. *J. Hydrol.* **2013**, *505*, 364–376, doi:10.1016/j.jhydrol.2013.10.013.

106. Manning, R. *On the flow of water in open channels and pipes*; 1891; Vol. 20;.

107. Musleh, F.A.; Cruise, J.F. Functional relationships of resistance in wide flood plains with rigid unsubmerged vegetation. *J. Hydraul. Eng.* **2006**, *132*, 163–171, doi:10.1061/(ASCE)0733-9429(2006)132:2(163).

108. Ballesteros, J.A.; Bodoque, J.M.; Díez-Herrero, A.; Sanchez-Silva, M.; Stoffel, M. Calibration of floodplain roughness and estimation of flood discharge based on tree-ring evidence and hydraulic modelling. *J. Hydrol.* **2011**, *403*, 103–115, doi:10.1016/j.jhydrol.2011.03.045.

109. Nepf, H.M. Drag, turbulence, and diffusion in flow through emergent vegetation. *Water Resour. Res.* **1999**, *35*, 479–489, doi:10.1029/1998WR900069.

110. Kouwen, N.; Unny, T.E. Flexible Roughness in Open Channels. *ASCE J Hydraul Div* **1973**, *99*, 713–728.

111. Wang, J.; Zhang, Z. Evaluating Riparian Vegetation Roughness Computation Methods Integrated within HEC-RAS. *J. Hydraul. Eng.* **2019**, *145*, 4019020, doi:10.1061/(ASCE)HY.1943-7900.0001597.

112. Freeman, G.E. *Determination of Resistance Due to Shrubs and Woody Vegetation*; ENGINEER RESEARCH AND DEVELOPMENT CENTER VICKSBURG MS COASTAL AND HYDRAULICSLAB, 2015;

113. Corenblit, D.; Tabacchi, E.; Steiger, J.; Gurnell, A.M. Reciprocal interactions and adjustments between fluvial landforms and vegetation dynamics in river corridors: A review of complementary approaches. *Earth-Science Rev.* **2007**, *84*, 56–86, doi:https://doi.org/10.1016/j.earscirev.2007.05.004.

114. Shih, S.F.; Rahi, G.S. Seasonal Variations of Flow Retardance in a Subtropical

Marsh. *Pap. - Am. Soc. Agric. Eng.* **1980**, *25*, 116–119.

115. Casas, A.; Lane, S.N.; Yu, D.; Benito, G. A method for parameterising roughness and topographic sub-grid scale effects in hydraulic modelling from LiDAR data. *Hydrol. Earth Syst. Sci.* **2010**, *14*, 1567–1579, doi:10.5194/hess-14-1567-2010.
116. Kean, J.W.; Smith, J.D. Form drag in rivers due to small-scale natural topographic features: 2. Irregular sequences. *J. Geophys. Res. Earth Surf.* **2006**, *111*, doi:10.1029/2006JF000490.
117. Laslier, M.; Hubert-Moy, L.; Dufour, S. Mapping riparian vegetation functions using 3D bispectral LiDAR data. *Water (Switzerland)* 2019, *11*.
118. Medeiros, S.C.; Hagen, S.C.; Weishampel, J.F. A Random Forest Model Based on Lidar and Field Measurements for Parameterizing Surface Roughness in Coastal Modeling. *IEEE J. Sel. Top. Appl. Earth Obs. Remote Sens.* **2015**, *8*, 1582–1590, doi:10.1109/JSTARS.2015.2419817.
119. Werner, M.G.F.; Hunter, N.M.; Bates, P.D. Identifiability of distributed floodplain roughness values in flood extent estimation. *J. Hydrol.* **2005**, *314*, 139–157, doi:10.1016/j.jhydrol.2005.03.012.
120. Cook, A.; Merwade, V. Effect of topographic data, geometric configuration and modeling approach on flood inundation mapping. *J. Hydrol.* **2009**, *377*, 131–142, doi:10.1016/j.jhydrol.2009.08.015.
121. Hunter, N.M.; Bates, P.D.; Horritt, M.S.; Wilson, M.D. Simple spatially-distributed models for predicting flood inundation: A review. *Geomorphology* 2007, *90*, 208–225.
122. Xiong, Y.F. A dam break analysis using HEC-RAS. *J. Water Resour. Prot.* **2011**,

3, 370.

123. Violin, C.R.; Cada, P.; Sudduth, E.B.; Hassett, B.A.; Penrose, D.L.; Bernhardt, E.S. Effects of urbanization and urban stream restoration on the physical and biological structure of stream ecosystems. *Ecol. Appl.* **2011**, *21*, 1932–1949.

124. Brunner, G.W. HEC-RAS, River Analysis System Users Manual.

2. JOURNAL ARTICLE: ESTIMATING FLOODPLAIN VEGETATIVE ROUGHNESS USING DRONE-BASED LASER SCANNING AND STRUCTURE FROM MOTION PHOTOGRAMMETRY

2.1 Background and Rationale

Riverscapes are dynamic, linear riverine systems characterized by high connectivity and spatial complexity (Figure 1) [1,2]. While riverscapes provide crucial economic and societal services, they also can be prone to flood hazards [3]. Changes in the hydrologic cycle due to climate change has resulted in increased heavy precipitation events and more extreme high-flow events in the Eastern United States [4]. The ability to accurately model floods will be of the utmost importance for management activities as we respond to the challenges regarding climate change [5]. In this study, we used remotely sensed data from unoccupied aerial vehicles (UAVs) to estimate vegetative roughness in the floodplain of a small mixed-use stream in Blacksburg, VA (Figure 2) with the overarching goal of improved hydrodynamic modeling.

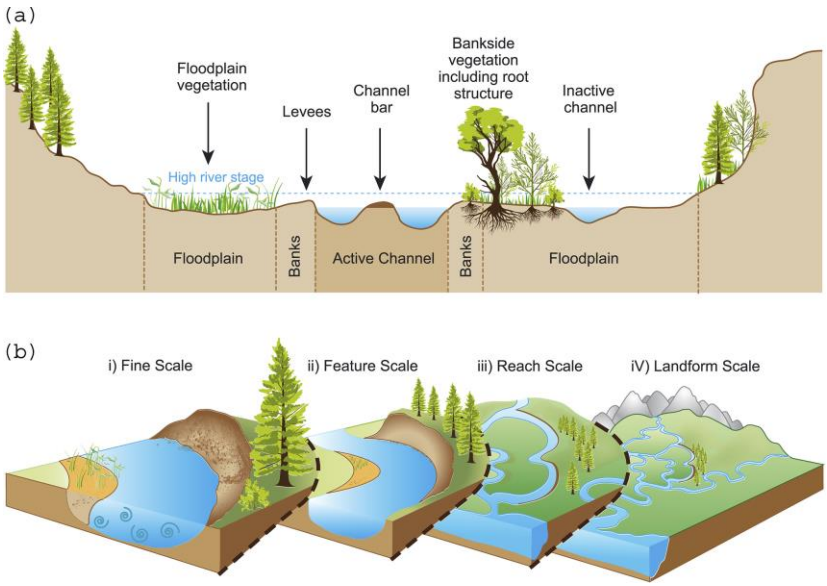

Figure 1. a. Key natural features of river coridors or riverscapes **b.** Range of scales relevant to riverscapes. From Tomsett and Leyland [3].

Figure 2. Flood event at the Stroubles Creek study site within the Virginia Tech StREAM Lab during the fall of 2019.

2.1.1 UAV Remote Sensing

Remote sensing techniques have been increasingly utilized to measure parameters related to ecological and hydrological function of riverscapes due to decreased costs and increased resolution [6]. Advancements in the technology and policy regarding UAVs, or drones, have made these systems useful to researchers in small- to medium-sized study areas (<1-10 km^2) [7]. UAVs are operationally more flexible and less expensive than aerial surveys (planes), and since they fly at lower altitude, the surveys produce data with higher resolution [8,9]. Of particular note for this paper, there has been interest in using UAV data for roughness estimates for use in hydrodynamic modeling [10,11].

2.1.2 Vegetative Roughness

Roughness coefficients represent the resistance to flow in channels and floodplains [12] and it is an important hydraulic characteristic, linked to water surface elevation and velocity [13]. The most widely-used roughness measure is Manning's roughness (*n*), which is utilized in Manning's equation (equation 1) for determining velocity and discharge in open channels [14].

$$Q = VA = \frac{1}{n} A\, R^{\frac{2}{3}} S^{\frac{1}{2}} \quad (1)$$

Where Q is discharge (m^3/s), V is velocity (m/s), A is cross sectional area (m^2), R is hydraulic radius (m), and S is slope (m/m).

Manning's roughness is the most sensitive variable in the equation, and one of the hardest to estimate [15]. In the past, roughness has been estimated by simple descriptions of channels and floodplains [16], or by comparing pictures to the landscape [17]. Chow [16], developed a roughness look-up table for different vegetation types in the floodplain (Table 2). Another method, developed by Cowen [18], distributes total roughness amongst important components: particle size, surface irregularities, shape and size of the channel cross-section, obstructions,

vegetation, and meandering. All these methods are highly subjective, and therefore have significant error associated with determining *n* [19]. While these techniques are still being used for basic estimations of roughness, new techniques have been developed to determine *n* in more quantitative, objective ways [20,21].

Table 2. Roughness look-up table developed by Chow [16]

Roughness in Floodplains	**Min *n***	**Max *n***
Pasture, no brush		
short grass	0.025	0.035
high grass	0.03	0.05
Cultivated Areas		
no crop	0.02	0.04
mature row crops	0.025	0.045
Brush		
scattered brush, heavy	0.035	0.07
light brush and trees, winter	0.035	0.06
light brush and trees, summer	0.04	0.08
medium to dense brush, winter	0.045	0.11
medium to dense brush, summer	0.07	0.16
Trees		
dense willows, summer, straight	0.11	0.2
cleared land with tree stumps	0.03	0.05
same as above, with heavy growth of sprouts	0.05	0.08
heavy stand of timber, a few down trees, little undergrowth, flood stage below branches	0.08	0.12
same as above, with flood stage reaching branches	0.1	0.16

Vegetative resistance is an important component of overall roughness and recent studies have improved roughness estimates influenced by vegetation [19–22]. Restoration of riparian or streamside forests has been a focus of stream restoration activities, and many efforts have been made to quantify their effects on water surface elevations and velocities [13]. Vegetation converts mean kinetic energy to turbulent kinetic energy in the channel, which affects drag and turbulence [23]. Studies involving flume and theory-based equations have been developed for submerged and non-submerged floodplain vegetation [24–26]. These equations, dependent on plant distribution and characteristics, have been applied to map the spatial distribution of roughness in a floodplain [20]. Abu-Aly et al. [22] found that adding spatially distributed vegetation roughness metrics in a 2D hydrodynamic model resulted in a significant decrease in mean velocity (-17.5%), and an increase in wetted area (8%) and mean depth in a channel (7.4%).

2.1.4 Comparing Drone Laser Scanning to Aerial Laser Scanning

One method of calculating vegetative roughness is to utilize data from Aerial Laser Scanning (ALS) [27]. Laser scanning, or lidar, is an active remote sensing method that typically uses pulsed near infrared lasers to calculate distances by measuring reflected time and utilizing the speed of light. There have been many environmental applications of ALS, such as measuring canopy heights [27,28], terrain modeling [29], and measuring vegetative density [30]. The ability of ALS to collect data across large areas is useful for measuring physical parameters of riverscapes such as stream gradient, width, and sinuosity [31]. While vegetative density is an important field-derived variable for many roughness equations [20], lidar-derived vegetative density has not been related well to field-derived vegetative density [30].

A method outlined by Mason [25] used ALS derived vegetation height to determine Manning's roughness in floodplains. However, ALS point densities are typically limited to 10 points/m^2, making it difficult to detect small changes in the vegetation and terrain, which may be important for roughness estimations [8]. Another lidar platform, DLS, is a novel method to measure riverscapes. Resop et al. [8] compared ALS to DLS and found a large increase in the amount of points classified as vegetation, from 2% to 12%. They found that DLS was more accurate in measuring heights, widths, and lengths of objects in the landscape such as bridges, and fences. Because of the increase in accuracy and the detection of more points, including vegetation points, they concluded that DLS better captured the spatial heterogeneity of both the terrain and vegetation [8].

DLS is uniquely positioned for measuring vegetative metrics as it allows for increased temporal (daily, monthly, seasonal flights) and spatial (more than 400 pts/m^2 at 30-m flight elevation) resolutions. Since UAVs fly at low altitudes, the data resolution is well suited for hard-to-scan areas along riverscapes such as steep streambanks and areas of dense vegetation [8]. The increase in resolution is also important for low-lying vegetation, and surface roughness, which are not as well detected by ALS or other remote sensing methods. DLS has been shown to have lower error than ALS at measuring height of a variety of vegetation types, which should lead to improved roughness estimates [7,32].

2.1.5 Structure-from-Motion Photogrammetry

In many studies, a UAV is paired with a camera as it is a more affordable option compared to lidar systems [9,32–35]. SfM photogrammetry can then be utilized to overlap the resulting aerial photos and create a point cloud of a landscape [34]. Past riverscape studies

involving UAVs have used SfM photogrammetry techniques to determine ecological and hydrological characteristics of riverscapes. SfM has been applied to mapping vegetation distribution [36], detecting large woody debris [37], and monitoring stream restoration [38]. Accuracy of SfM point clouds can be improved with the use of ground control points (GCPs), which are surveyed points that can be seen in the aerial images [39]. Generally, 10 randomly dispersed GCPs are recommended per flight [37]. Unlike lidar, camera images can have difficulty penetrating through vegetation, thereby limiting the number of ground points in the point cloud [33]. This can result in errors of heights of objects (including vegetation) within the point clouds in highly vegetated areas [34]. The resulting products from these SfM products (e.g., Digital Elevation Models (DEM) and Canopy Height Models (CHM)) are prone to errors which can propagate through to estimates of roughness [39]. This could be improved by using ALS derived DEMs instead, which would have better ground coverage, but the vegetation less so.

2.1.6 2D Hydrodynamic Modeling

Past studies have used stage-dependent roughness factors within high-level 2-D hydrodynamic modeling [27,40,41], some with field-derived vegetation measurements such as drag coefficients [20]. Studies have utilized a variety of 2D hydrodynamic models, such as Telemack 2D [40], MIKEFLOOD [42], RIVER2D [41,43] and SRH-2D [22]. In this study, we utilized 2D HEC-RAS, a model developed by the U.S. Army Corps of Engineers (USACE), commonly used for water resource projects such as flood maps [44], dam removal projects [45], and stream restoration projects [46]. 2D HEC-RAS utilizes the Saint Venant equations to predict unsteady flow [47]. It takes advantage of high-quality remotely sensed datasets to create spatially variable outputs, such as water surface elevations, velocities, flood extents [22].

2.1.7 Goal and Objectives

We utilized vegetation heights derived by high resolution DLS and SfM datasets to estimate vegetative roughness for a floodplain of a small third-order stream in Blacksburg, Virginia. These roughness estimates were then utilized in the 2D HEC-RAS hydrodynamic model. 2D HEC-RAS can only utilize a static roughness raster that is not stage dependent [47]. We used three different roughness estimation techniques (Constant n, Chow, and Mason) to create calibrated HEC-RAS models to compare to field measurements of seven flood events in Fall 2018 and Fall 2019. The first two roughness techniques derived *n* from a lookup table (NLCD and Chow) and then calibrated these values to fit a velocity probe. The last technique, developed by Mason et al. [27], relates vegetation heights to Darcy-Weisbach friction coefficients, which can be converted to determine Manning's roughness. All these methods are assumed to improve hydrodynamic modeling and can create useful outputs such as rating curves to improve future analysis of the riverscape. In summary, the specific objectives of this research were:

1. Evaluate 2D hydrodynamic model simulations of floods using roughness estimated based on DLS-based point clouds.
2. Evaluate 2D hydrodynamic model simulations of floods using roughness estimated based on SfM-based point clouds.
3. Compare 2D hydrodynamic modeling simulations using DLS-based versus SfM-based roughness estimates.

2.2 Methods

2.2.1 Study Area

The Virginia Tech Stream Research, Education, and Management (StREAM) Lab (https://vtstreamlab.weebly.com/) is along a 1.7-km reach of Stroubles Creek downstream of the Virginia Tech Campus in Blacksburg, VA (Figure 3) [48]. Stroubles is a gravel-bed stream, whose headwaters are located entirely in the Town of Blacksburg and the Virginia Tech campus (Figure 2). The watershed upstream of the study area is 14.5 km^2 and is 89.5% urbanized [49]. Because of the urban nature of the watershed, there are many high flows in the study area, leading to flooding, erosion, and other issues. Due to the aforementioned issues, Stroubles Creek has been on the U.S. Environmental Protection Agency's 303(d) list of impaired streams since 2003 [50].

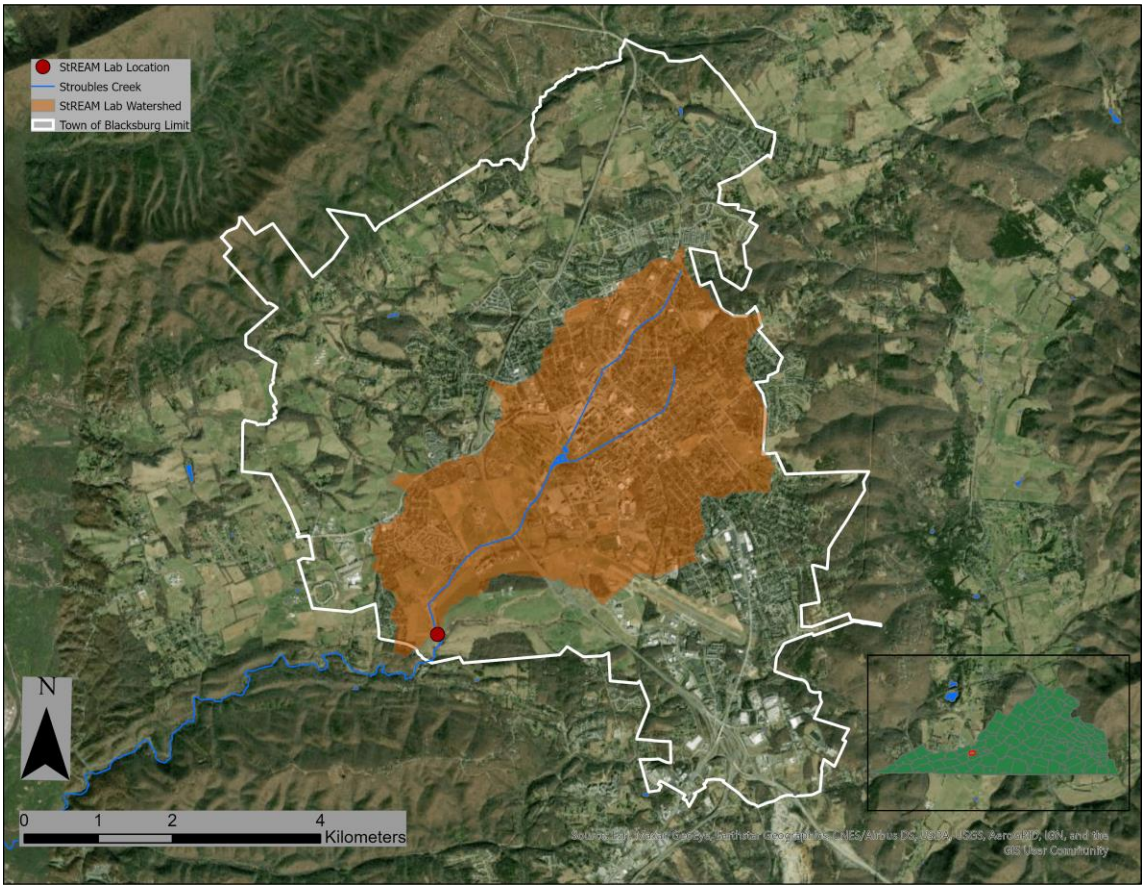

Figure 3. StREAM Lab location and Stroubles Creek watershed in Blacksburg, Virginia.

During 2008-2010, 2.1 km (1.5 mi) of Stroubles Creek and Docs Branch (a small tributary) were restored at the StREAM Lab utilizing three different techniques [51]. The actual construction activities focused on the section between sampling Bridge 1 and Bridge 3 (Figure 4). The section between Bridge 1 and Bridge 2 involved regraded vertical streambanks to a 3:1 slope and planting native riparian vegetation, while the section between Bridge 2 and 3 utilized a natural channel design that included installing inset floodplain as well as grading streambanks to 3:1 slopes [51]. The restoration project increased floodplain connectivity and vegetative complexity particularly between the concrete bridge and Bridge 3 [52]. Due to increased amount of out of channel flows from the restoration in 2010, we chose this section of the StREAM Lab to evaluate vegetative roughness.

Figure 4. Map of the Virginia Tech StREAM Lab, with the project extent shown in red.

2.2.2 Data Collection

2.2.2.1 Field Data

At the StREAM Lab, there is on the ground monitoring to assess the long-term effects of the stream restoration completed in 2010. In the study area, there is a monitoring bridge (Bridge 2) continuously measuring stage and water-quality parameters. There are 18 wells with pressure transducers, measuring water elevations every 15 min (Figure 5). Well data has been taken at the

flood peaks of the measured floods determined by the bridge 2 (Table 3). Measured floods were picked in Fall of 2019 and 2018 to minimize seasonal effects of roughness. Velocity probes have been deployed upstream of Bridge 2 to measure velocity and water surface elevation, one in the channel and one in an inset floodplain (Figure 5). The velocity probes measured a variety of floods in fall 2019 and created an acceptable range of water surface elevations and velocities. Lastly, the flood extents of the flood that occurred on 10/11/2018 (Table 3) had been flagged and surveyed to determine water surface elevations at the peak flow throughout the study area. Field data were used to calibrate (velocity probes) and validate (wells, flood extents) the roughness metrics derived from photogrammetry and lidar techniques.

Table 3. Measured Floods, fall 2018 and fall 2019

Date	Bridge 2 Stage (m)	WSE (m)
9/17/2018	1.26	604.36
9/23/2018	1.53	604.64
9/28/2018	1.37	604.47
10/11/2018	1.52	604.62
10/20/2019	1.32	604.42
10/27/2019	1.23	604.33
10/31/2019	1.52	604.63

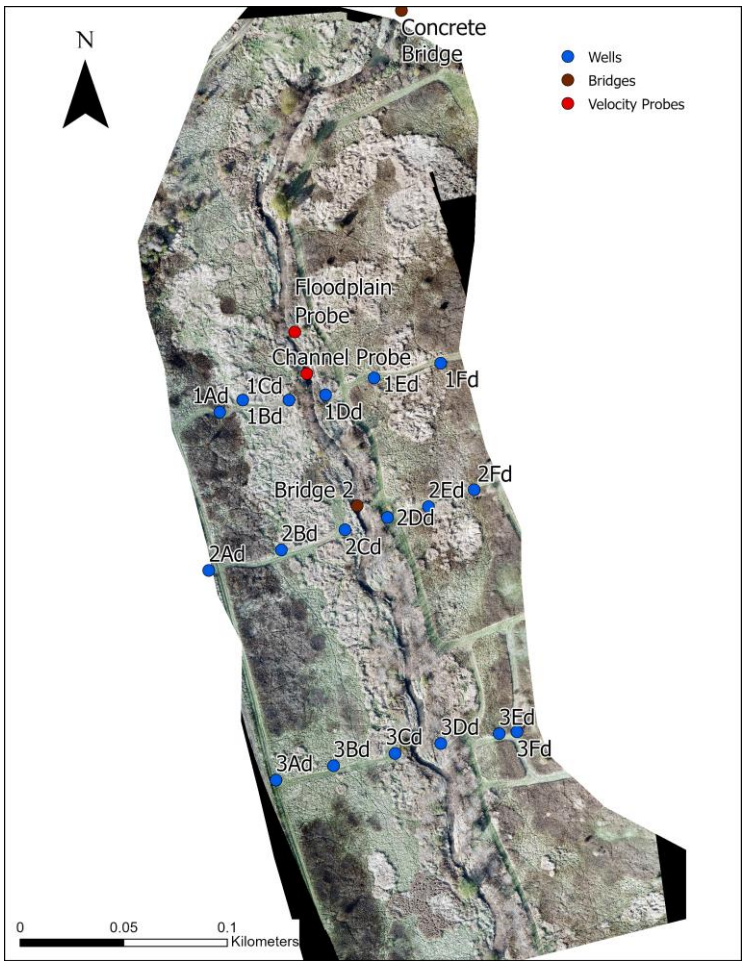

Figure 5. Well, bridges, and velocity probe locations in the study area. Photogrammetric image showing the vegetative complexity of the study area.

2.2.2.2 DLS Data and Processing

The UAV system utilized for lidar surveys in this study is a Vapor35 (AeroVironment, Simi Valley, California) with a Yellowscan Surveyor Core lidar unit (Monfeerier-sur-Lez, France) (Figure 8a). The lidar unit consists of a Velodyne VLP-16 laser scanner (San Jose, CA) and a Trimble APPLANIX APX-15 GNSS-inertial (Richmond Hill, Canada). To plan and conduct Vapor35 flights, we use the wePilot1000 flight control system and the weGCS ground control system software (weControl SA, Courtelary, Switzerland). The lidar flights were flown at

a 30 m altitude, with 20 m flight-line spacing, which was recommended by Yellowscan Staff for optimum point spacing and density. The lidar flight was conducted in Fall 2018.

The YellowScan system is ultralight, 2.1 kg, which is the allowable payload limit for the Vapor35. The lidar can record two returns per pulse and uses a wavelength of 905 nm. The Velodyne puck and the APPLANIX unit allow for one button data acquisition. After a flight, data was corrected using a local CORS base station, and is outputted into a LAS file format in UTM zone 17N.

2.2.2.3 SfM Data and Processing

The UAV system utilized for collecting aerial imagery was a DJI Mavic Pro (DJI, Shenzen, China) with a camera (Figure 8b). According to the DJI website, the camera specifications are 1/2.3" (CMOS), Effective pixels:12.35 M (Total pixels:12.71M). The DJI Flight Mapper (AeroScientific, Adelaide, Australia) application was utilized to create flight maps in the study area, while the Litchi (VC Technology, London, U.K.) application was used to conduct the pre-programmed flights. Flights were conducted at midday to minimize shadow effects on the images. The study area had to be broken up into 3 flights due to flight motor battery constraints, with the camera at 90-degree angle. Flights were flown at 36.5 m with settings recommended by the DJI Flight Planner application. A 4th flight was flown over the entire study area at 61 m with the camera at 75 degrees. Flights flown at different angles and altitudes have been determined to create more accurate point clouds, as it creates a more convergent view of the landscape [53,54]. Images were taken every 2 seconds to ensure an 80% overlap to improve the accuracy of the point cloud. The photogrammetry flight was conducted in Spring, 2020.

The images acquired from the flight were then processed in Agisoft Metashape (St. Petersburg, Russia). A standard workflow was used: importing the UAV images, initial processing, importing the ground control points, and creating a dense point cloud. Bowling balls placed on rebar were used as ground control points (Figure 7). This process resulted in a point cloud in LAS file format in UTM Zone 17N.

Figure 6. An example of a ground control point used in this study.

(**a**) (**b**)

Figure 7. (**a**) Vapor 35 shown with laser scanner payload. (**b**) DJI Mavic Pro 2 with 4K camera.

2.2.2.4 Point Cloud Products

Lidar and SfM point clouds were not adequate for producing bathymetry measurements: therefore, we conducted a detailed survey of the below-water stream channel with a Trimble R12 GNSS System (Sunnyvale, California, USA) to fill in the data gaps. LAStools (rapidlasso GmbH) are script-batchable command line tools used to classify point clouds. They were used to classify the ground points of the point clouds using the LASground tool in LAStools. ArcGIS Pro (ESRI, Redlands, California, USA) was used to manually classify building points, such as bridges and other manmade objects. All other above-ground points were considered vegetation, with a 0.1 m buffer to account for uncertainty between the ground and the low vegetation. This classification of vegetation points, height normalization using the ground points, and creation of a Canopy Height Model were performed using the LASheight and LAS2dem tools in LAStools. The CHM pixel size was set to 0.1 m to take advantage of the high-resolution data of both point clouds.

2.2.3 Hydrodynamic Modeling

The data analyses and modeling process is illustrated in Figure 8. After data collection activities (discussed above) we set up a 2D HEC-RAS model to simulate flooding at the study site using the three different Manning's roughness estimation methods (constant, Chow, and Mason), or five different roughness inputs since Chow and Mason methods were developed twice each from the DLS and SfM data.

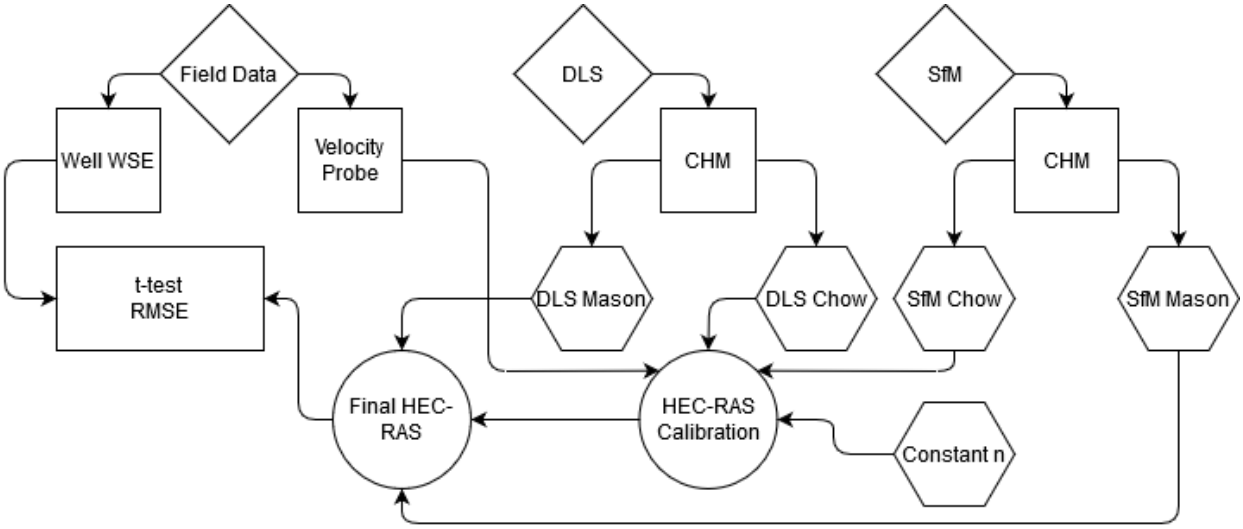

Figure 8. Workflow to produce, calibrate, and validate 2D HEC-RAS models using UAV derived data and field data.

2.2.3.1 2D HEC-RAS Model Set Up

2D hydrodynamic modeling was used to predict flood extent and flow velocities at discharges in a stair step method, with an increase in discharge every model day [47]. This ensured that steady state conditions were achieved before flows inundated the floodplain. Inputs for HEC-RAS included a DEM, the downstream slope, a flow area to create a mesh of calculation points created in the program, upstream and downstream boundary conditions for the flow area (Figure 9), a series of flows, and a roughness raster. In this study, the 2D mesh

contains 1 m^2 cells, each containing a calculation point. The grid mesh had break-lines of the channel and the inset floodplain to align the mesh to the topography. This will help minimize water leakage through a bank within a cell during a simulation [47]. The 2D HEC-RAS software allows for roughness inputs as a raster layer. In this study, we calibrated roughness values for Constant n, and Chow method by comparing 2D HEC-RAS outputs to measured flood events in the field.

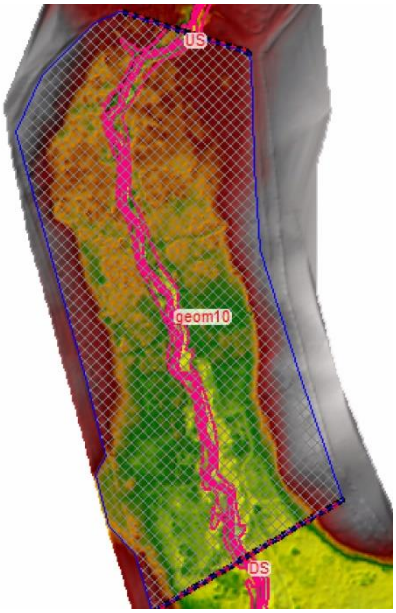

Figure 9. The 2D HEC-RAS generated grid mesh covering the study area, showing the upstream and downstream boundary conditions (pink and black lines), and the break lines (pink lines).

2.2.3.2 Roughness Determination and Calibration

To create a raster data layer of hydraulic roughness, different roughness estimation techniques were implemented (hexagons in Figure 8). For the first method, hereafter referred to as the "Constant *n*" method, we used a uniform roughness, one value in the channel and one value in the floodplain. To develop starting *n* values, we utilized NLCD landcover data from 2016 to determine a single value roughness in the floodplain [55]. According to the most recent

NLCD data (2016), the study area is entirely classified as pasture/hay, with an estimated *n* of 0.025 – 0.05 (Table 4). However, the area currently better fits the criteria scrubland or deciduous forest, *n* = 0.07 – 0.16 (Table 4). This discrepancy is due to its history as pasture, and the relatively recent restoration efforts fencing off cattle and planting trees along this stream reach. Using this information, a reasonable starting point for the analysis was an *n* of 0.035 in the channel and 0.1 in the floodplain.

Table 4. Roughness ranges for NLCD values.

Landcover Type	NLCD Roughness Values
Mixed Forest	0.10 - 0.16
Shrub/Scrub	0.07 - 0.16
Pasture/Hay	0.025 -0.05

After running the 2D HEC-RAS model, the simulated water surface elevations (WSE) and velocities were compared to velocity probe data at the actual flood peaks to calibrate the Manning's *n* in the channel and in the floodplain (right circle in Figure 10). The velocity probe data were in lieu of stage-discharge data from a USGS gage, or another data source, which are commonly used to calibrate HEC-RAS models [20]. Due to our focus on floodplain roughness, the roughness values were calibrated to the velocity probe in the inset floodplain. The velocity probe WSEs and velocities were graphed, giving a range of data over many months of observation. The model WSE and velocity that fit inside this range the best, by looking at the graph, was considered the calibrated model.

For the second method, hereafter referred to as the "Chow" method, we created a roughness raster layer derived from Chow's [16] roughness developed for floodplain vegetation (Table 1). Using a Canopy Height Model (CHM), vegetation height ranges were used to

reclassify pixels into vegetative groups: grass, scrub, tree and large tree (Figure 6). This vegetation was then reclassified to Manning's *n* using the lookup table (Table 1) [16]. Table 5 shows the reclassification criteria using the CHM, as well as the values determined using the lookup table. As in the previous method, the model was then calibrated by changing the roughness parameters to better fit the velocity sensors.

Table 5. Reclassification criteria and corresponding *n* values from Chow [16].

Vegetation Type	**Min Height (m)**	**Max Height (m)**	**Chow *n***
Grass	0	1	0.05
Scrub	1	2.5	0.07
Tree	2.5	5	0.16
Large Tree	5	20	0.20

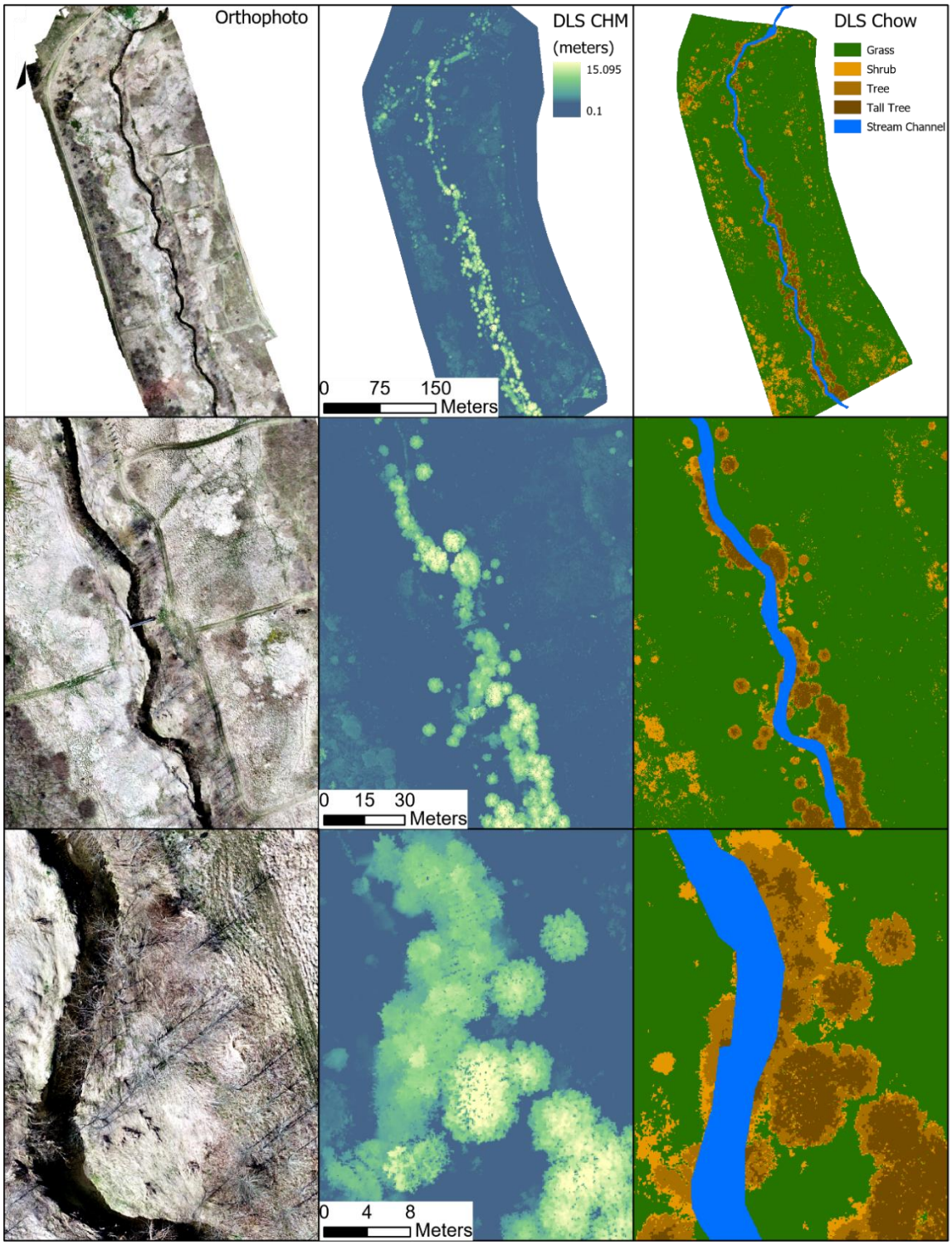

Figure 10. Maps showing a SfM derived Orthophoto, DLS derived CHM, and Reclassified DLS CHM (Chow) at different spatial scales from top to bottom.

The third method was a simplified version of an approach developed by Mason [27], hereafter referred to as the "Mason" method. The Mason method simplified flume and theoretical relationships, to only need vegetative heights to solve for Darcy-Weisbach friction coefficients. The friction coefficients were then converted to *n*, using a relationship developed by Fathi-Maghadam and Kouwen [26]. This method assumes similar rigidity, shape, and momentum absorptivity of vegetative classes to avoid the need for extensive field work to determine individual plant properties [56]. Since this HEC-RAS model cannot utilize stage dependent roughness, typical values were used for the depth and velocity to determine the friction values, similar to what was employed by Hopkinson et al. [56]. Formulas have been developed for short submerged vegetation less than 1 m (Equation 2) [25,57], and non-submerged medium to tall vegetation (Equation 3) [26] to predict the Darcy-Weisbach friction coefficient, *f*. To get equations 2 and 3 to work in unison, the Con tool in ArcGIS Pro was employed to apply equations above and below 1 m. The formulas from Mason are as follows:

$$f = 4.06\left[\frac{V}{\sqrt{\frac{\varepsilon E}{\rho}}}\right]^{-0.46}\frac{y_n}{h} \tag{2}$$

$$\frac{1}{\sqrt{f}} = a + b\log(\frac{y_n}{k}) \tag{3}$$

Where V is the flow velocity (m/s), y_n is the normal depth (m), h is the vegetation height (m), εE is a measure of the trees elastically (N/m^2), and k is the deflected grass vegetation height (m). The variables a and b are related to the boundary shear stress.

As in Mason et al [27], elasticity values determined by Kouwen and Fathi-Moghadam [26] were used. The εE selected was white pine, lying in the midrange of the coniferous trees studied. Since 2D HEC-RAS cannot utilize stage dependent *n*, values of 1 m and 0.05 m/s were used for normal depth and velocity. These were typical values found in the results of the

previous methods. The final raster of n was calculated using the friction coefficient (Equation 4) [27]. Since this is a calculated roughness, it does not need to be calibrated like the first two methods [27]. This roughness raster was subsequently added and run in HEC-RAS for further analysis. Assuming that the hydraulic radius equals the normal depth, Manning's roughness was determined using a relationship developed by Fathi-Maghadam and Kouwen [26]:

$$n = \sqrt{\frac{f\, y_n{}^{1/3}}{8g}} \tag{4}$$

where g is the gravitational acceleration constant.

The second and third methods were repeated with the UAV SfM photogrammetry data. To ensure spatial consistency, the SfM point cloud was aligned to the lidar point cloud using the align tool in CloudCompare (https://www.danielgm.net/cc/). This was then put through a similar workflow to the lidar point cloud to create a CHM using the ground points and vegetation points from the SfM las file. This CHM was then used to produce roughness rasters using the Chow and Mason methods listed above. Since the datasets were similar, the calibrated DLS Chow roughness values were used for SfM Chow. To focus the study on vegetation roughness, the DLS DEM was used for all models, to ensure that the roughness parameter was the only changing variable between each model.

2.2.4 Model Evaluation

For each model, WSE data were taken from every well point for each corresponding real flood peak. This was done by matching the WSE of the in-channel velocity probe with the same WSE at the location of velocity probe in the model to get a model time. Then, model WSE data were extracted at each well point with the corresponding model times for each real flood. The data was then the basis for the statistical analysis for this study.

To evaluate model simulations, we compared predicted versus measured water surface elevations for the seven flood events, a *t*-test with a 5% significance level was used. The null hypothesis tested was that there is no significant difference between the well water levels and the corresponding modeled water levels. This method was used by Cobby et al. [58] in a similar study to validate constant and variable friction 2-D hydrodynamic model outputs compared to synthetic aperture radar-derived flood extents. A two-sided *t*-test was used, as the well data is correlated to points in the model. The *t* values are given by

$$t = \frac{(\mu_1 - \mu_2)}{\sqrt{(s_1^2 - s_2^2 - 2\rho s_1 s_2)/N}} \quad (5)$$

where $\mu_1$and μ_2 are the means of the model and the well data, $s_1$and s_2 are the standard deviations, and ρ is the correlation coefficient between the model and well heights, and N is the number of wells.

To assess which model better predicts floods, we compared well WSE to the model WSE at each real flood peak using the root mean square error (RMSE), which is a common way of validating data [34]. RMSE is given by

$$RMSE = \sqrt{\frac{1}{n}\sum_{i=1}^{n}(Predicted_i - Actual_i)^2} \quad (6)$$

where predicted data is the model WSE elevation at well locations, actual is field derived well WSE, and n is the number of wells.

2.3. Results and Discussion

2.3.1 Flood Simulations Utilizing Constant n and DLS Chow Before and After Calibration

Two of the roughness methods used, Constant *n* and DLS Chow, needed to be calibrated to better fit the field data. Calibrating to the floodplain velocity probe, the best fit for the

Constant *n* method in the channel and floodplain were 0.04 and 0.5, respectively, compared to an *n* of 0.035 and 0.1 determined from the NLCD look up table. The initial and the final simulated water surface elevations, velocity with velocity probe data, and the model fit are provided in Figure 11. As mentioned previously, the velocity probe dataset is a range of storms in Fall 2019, while the HEC-RAS model uses a stair step method to increase floods gradually. The best fit was the model that had velocity and WSE elevations fit in the floodplain velocity probe's range. The higher roughness best fits the WSE of the velocity probe.

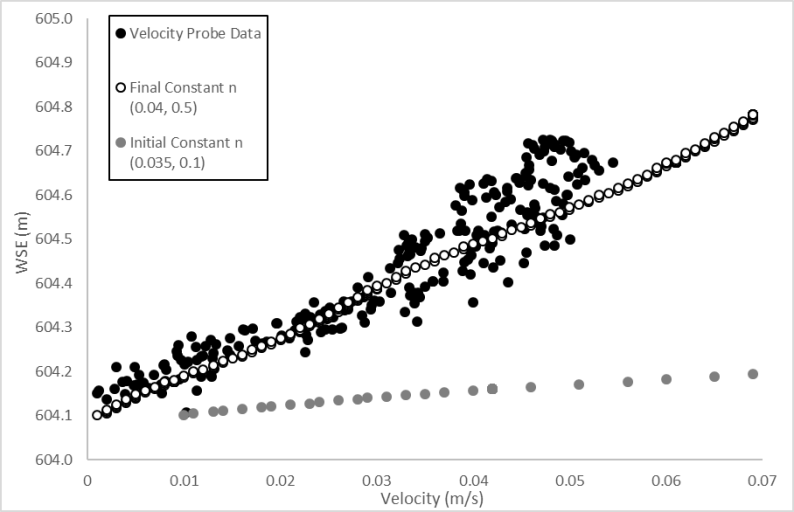

Figure 11. Comparing WSEs of the original versus the calibrated HEC-RAS runs of the Constant *n* method at the floodplain velocity probe.

For the Chow method we incorporated more spatial variability in the floodplain by identifying four groups of roughness instead of one. Similar to the Constant *n* method, there was a drastic increase in the floodplain roughness from look up table *n* values compared to final calibration values. The differences between the lookup table and the calibrated values are shown in Table 6, while the simulated WSE (pre and post calibration) and velocity probe WSEs are shown in Figure 12.

Table 6. Chow lookup table and calibrated values by vegetation type.

Vegetation Type	Chow *n*	Calibrated *n*
Grass	0.05	0.4
Scrub	0.07	0.45
Tree	0.16	0.5
Large Tree	0.2	0.6

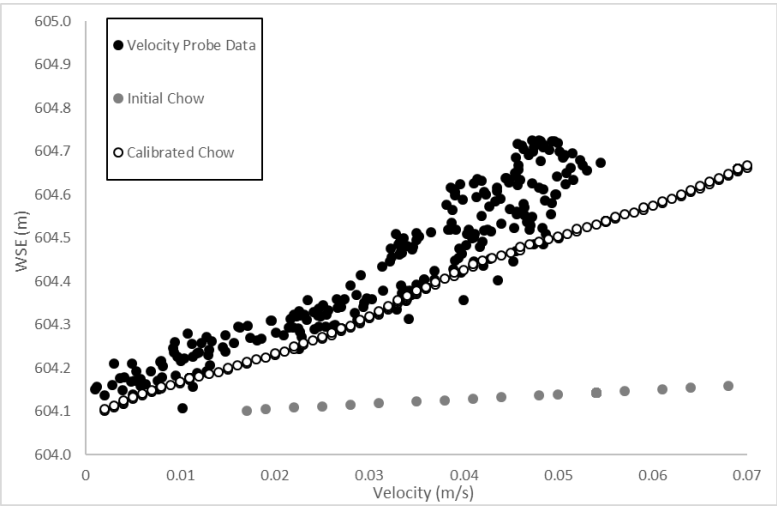

Figure 12. Comparing WSEs of the original versus the calibrated HEC-RAS runs of the DLS Chow method at the floodplain velocity probe.

For both the Constant *n* and the Chow methods, there is a large increase of *n* comparing the lookup table values to the calibrated results. For the Constant *n* roughness estimates, floodplain roughness was increased by a factor of 5. For the Chow method, the roughness was increased by a factor of 3 to 6, depending on vegetation type. This is consistent with the findings of Watson [59] who estimated that vegetation resistance values should be increased by a factor of 4 to 7.5 when comparing table values to field estimated values. Green [19], determined *n* values of 0.3 – 0.5 in a channel area using plant blockage values that was determined to be 0.1 using the Chow look up table. Another study compared calibrated HEC-RAS *n* values to field-

derived *n* values [60]. They found that calibrated *n* values overpredicted field derived values, especially in areas of heavy vegetation. Both the NLCD and Chow look up tables seemed to underpredict the vegetative roughness in the floodplain and would result in underpredicted flood depths in hydrodynamic models.

2.3.2 Evaluation of Flood Modeling using DLS Derived Roughness

The extent of inundation was flagged during shortly after a flood peak and surveyed the flood to identify flood extent during Fall 2018 (10/11/18) (Table 3). It had a peak stage of 1.53 m (based on bridge 2 stage recorder), and efforts were taken to flag the flood as close to the peak as possible (Table 3). The flood peak was matched up with the corresponding WSE in the simulated output. The flagged points were then snapped to the closest stream center points using survey points. These flagged elevations were compared to the Water Surface Elevations at each center point using data from each DLS model (Figure 13).

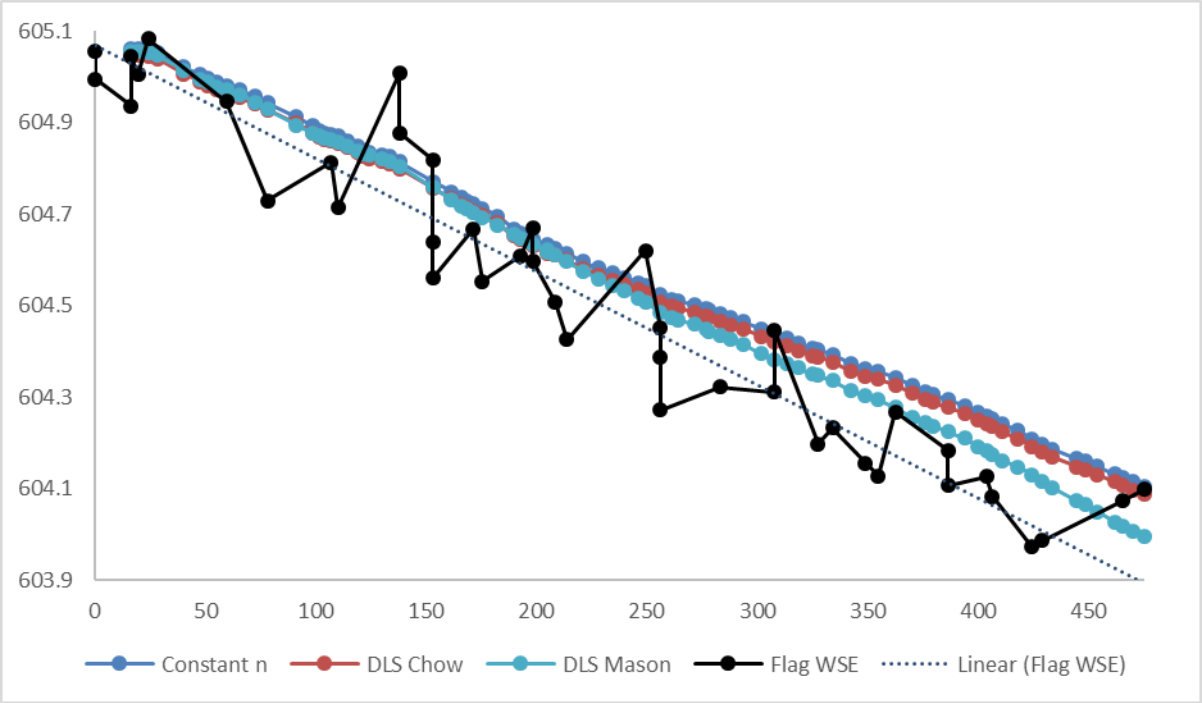

Figure 13. Comparison of flagged, Constant *n*, DLS Mason, and DLS Chow downstream WSE.

In Figure 13 the flagged flood generally shows a lower water surface elevation than the model results. While the flagging method has some error, such as difficulties seeing the flood in areas with thick vegetation and the fact that the flagging method takes time, so it did not capture the true peak or were they all placed at the same time. However, this does indicate that the Mason method is closer to the field-derived data.

The DLS Mason method predicted the WSE elevations better than the calibrated models (DLS Chow and Constant n). Most of the DLS Mason points are closer to the equal value line (Figure 14) and the DLS Mason method had a lower RMSE (-0.02 m; Table 7). The DLS Mason method does not require a gage to calibrate to, meaning it could be applied to areas without traditional monitoring and reduces the amount of time running the models to calibrate. In our case, individual model runs took an upward of 6 hours using a high-end desktop computer and needed multiple runs each time to calibrate to the velocity probe.

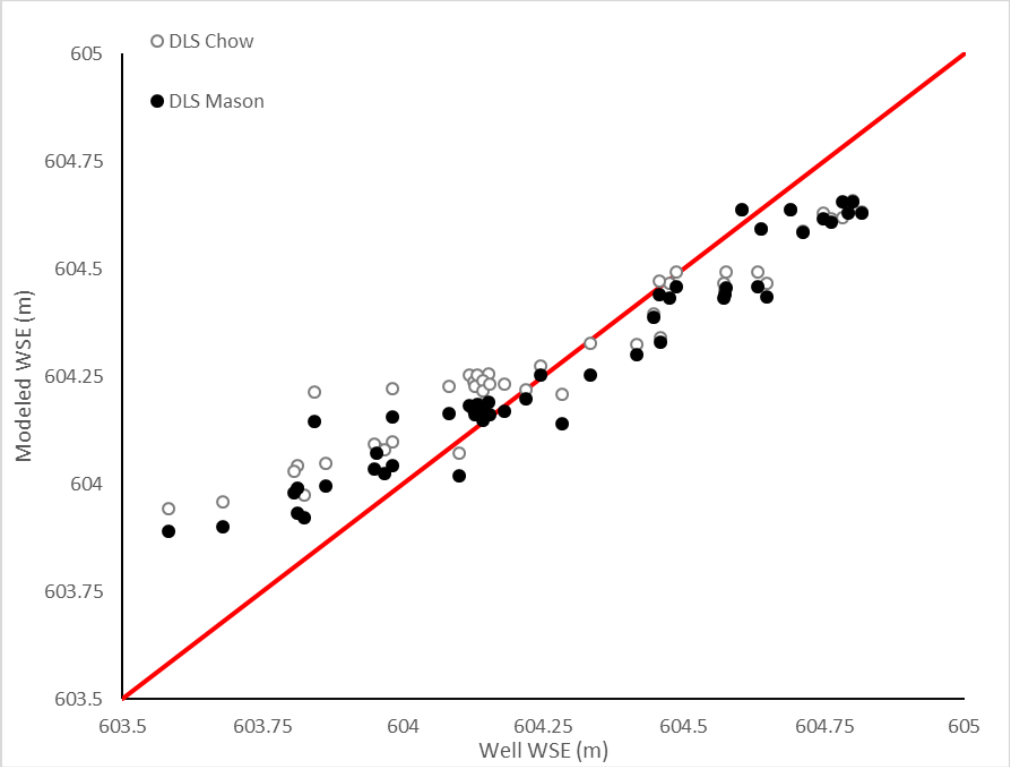

Figure 14. Comparing DLS Chow and DLS Mason simulated WSE.

Table 7. Statistics for DLS model runs and Constant n

Model Run	RMSE (m)	*p*	r^2
Constant n	0.146	0.064	0.93
DLS Chow	0.145	0.075	0.94
DLS Mason	0.124	0.853	0.94

When the *t*-tests were conducted, there were 50 degrees of freedom due to some gaps in the data. According to the *t*-tests, all model-derived WSEs were not statistically significant from the well-derived WSEs, with *p*-values greater than 0.05 (Table 7). Also, all model values are strongly correlated, with r^2 values between 0.93 and 0.94. This is an improvement over previous ALS studies, such as Cobby et al. [58], who found Constant *n* model runs had p-values less than 0.05. This is also an improvement over Abu-Aly et al. [22], another ALS study, who reported an r^2 of 0.6. Therefore, utilizing high-resolution DLS data for model inputs, such as the DEM, appears to improve hydrodynamic simulations.

2.3.3 Evaluation of Flood Modeling using SfM -Derived Roughness

The process was repeated using the SfM models. The results are shown in Figure 15. While there are concerns with the flagging method, the general trend of the flags clearly shows that the Mason method is clearly closest to this field derived dataset.

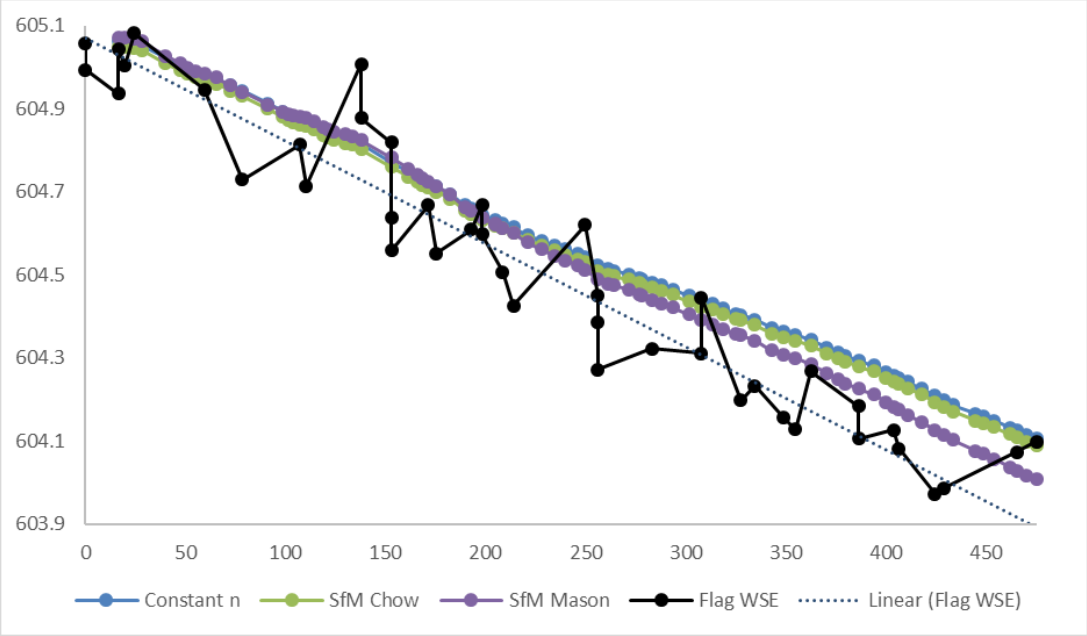

Figure 15. Comparison of flagged, Constant *n*, SfM Mason and SfM Chow downstream WSE.

The simulations using SfM data follows a similar trend of the simulations using DLS data when comparing SfM Chow to SfM Mason (Figure 16). The SfM Mason had a slightly smaller decrease in RMSE (0.01 m) compared to both Constant *n* and SfM Chow models (Table 8). The SfM Mason RMSE (0.136 m) is slightly higher than that reported by Tamminga et al. [41] where they used photogrammetry to create 2D hydrodynamic model inputs, and reported a RMSE of 0.125 m. Their study area was for a braided channel, that appeared to have less vegetation in their flow area. A caveat of this data analysis is that the DLS DEM was used for the SfM model runs. This was to ensure that the only changing variable in the model is the roughness itself.

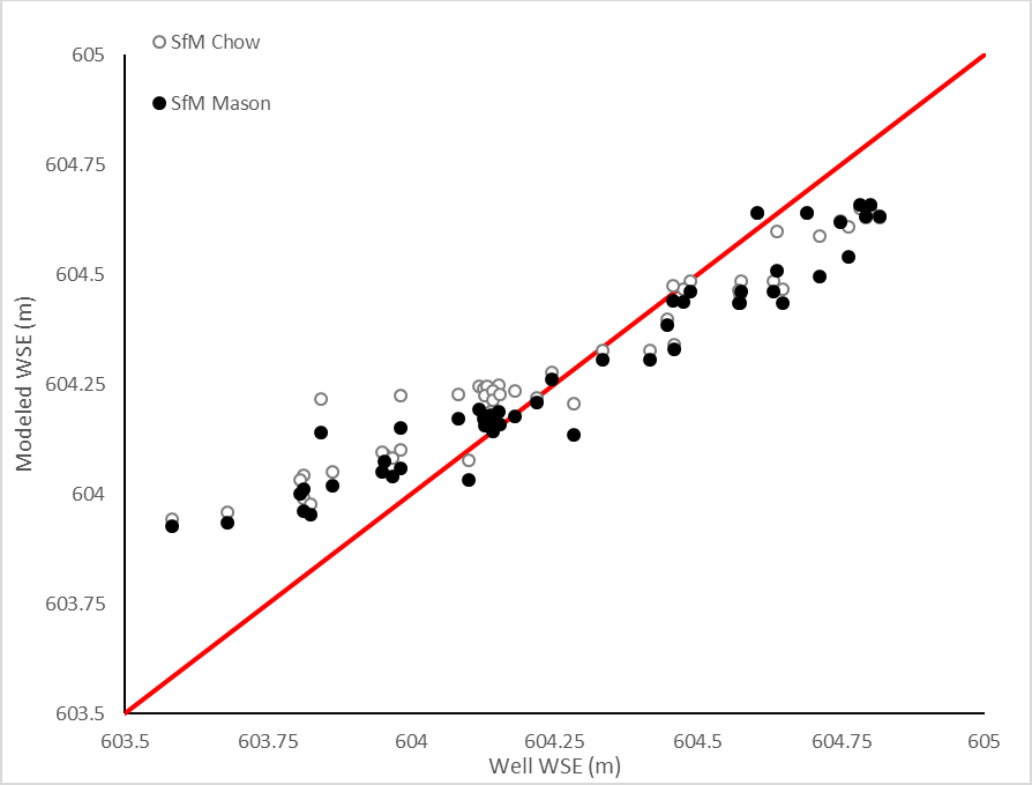

Figure 16. Comparing SfM Chow and SfM Mason simulation results.

Table 8. Statistics for SfM model runs and Constant *n*

Model Run	RMSE (m)	*p*	r^2
Constant n	0.146	0.064	0.93
Chow SfM	0.146	0.075	0.94
Mason SfM	0.136	0.959	0.94

2.3.4 Comparison of Flood Modeling using DLS and SfM Derived Roughness

To visually compare the SfM and DLS point clouds, a CHM of difference was made between the DLS and SfM data (Figure 17). The map is a color ramp, red areas indicate where DLS predicted higher vegetation heights and purple areas indicate areas where SfM photogrammetry had higher vegetative heights. A histogram showing the distribution of the differences between the DLS and SfM derived CHMs is provided in Figure 18. The vast majority of pixel values were within 0.4 m of each other, with the mean being -0.125 m. On average, the SfM data predicted higher vegetation heights compared to DLS. This might be obscured somewhat by the SE edge of the study area, which likely did not have the required photo density to adequately pick up the correct heights.

Differences occur mostly in areas on the edges of trees. This can stem from the error of SfM photogrammetry heights in highly vegetated areas, such as in the riparian areas in the study area. The figure also shows that the lidar picks up some of the emergent vegetation between in the edge of the floodplain further away from the channel. Figure 18 shows most of the pixel counts being close to 0 between the DLS minus the SfM CHMs, meaning the SfM does an adequate job of measuring vegetation height. For more detailed analysis determining the

accuracy of UAV derived vegetation height, the reader is directed to the work done by Kucharczyk et al. [7] for DLS and Dandois and Ellis [33] for SfM photogrammetry.

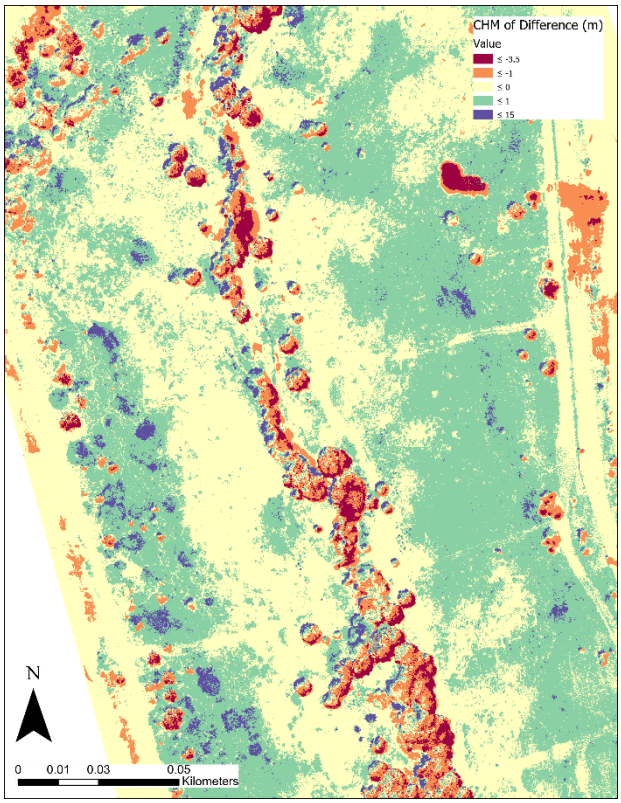

Figure 17. Map of CHM of Difference (DLS-SfM).

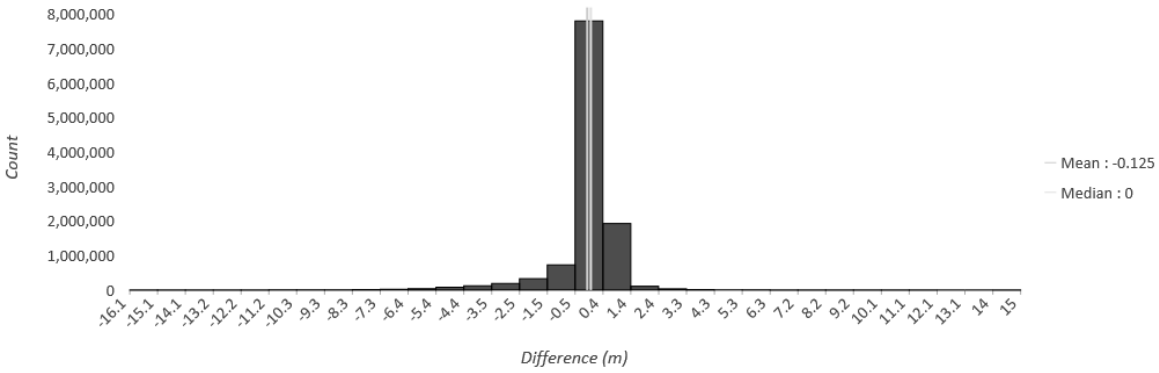

Figure 18. Distribution of the count of pixel values of the CHM of difference between DLS and SfM.

Both the DLS and SfM roughness rasters created by the Mason method had *n* values ranging from 0.05 - 0.92 (Figure 19). Most values were 0.05, which represents bare earth, or very short (<0.1 m) vegetation. These values are consistent with the findings of Mason et al. [27], who reported floodplain *n* values ranging from 0.07 to 0.83 at high stage (depths around 1 m in the floodplain). Because the normal depth was set to 1 m, the tall grass around 1 m had the largest *n* values. This is also due to the breakup in vegetation class by the two formulas. Equation 2, for vegetation above 1 m, has an increase in roughness with decreasing vegetation, meaning 1 m would have the highest roughness. Equation 3, vegetation less than 1 m, has an increase in roughness with an increase in vegetation, meaning its maximum would also be at 1 m. This means that grass around 1 m would have the highest values. Trees receive values in the 0.6 range, which is much higher than lookup table values, which are around 0.1. Also notable is that the lowest value, 0.05 is what is normally used for bare roughness without vegetation.

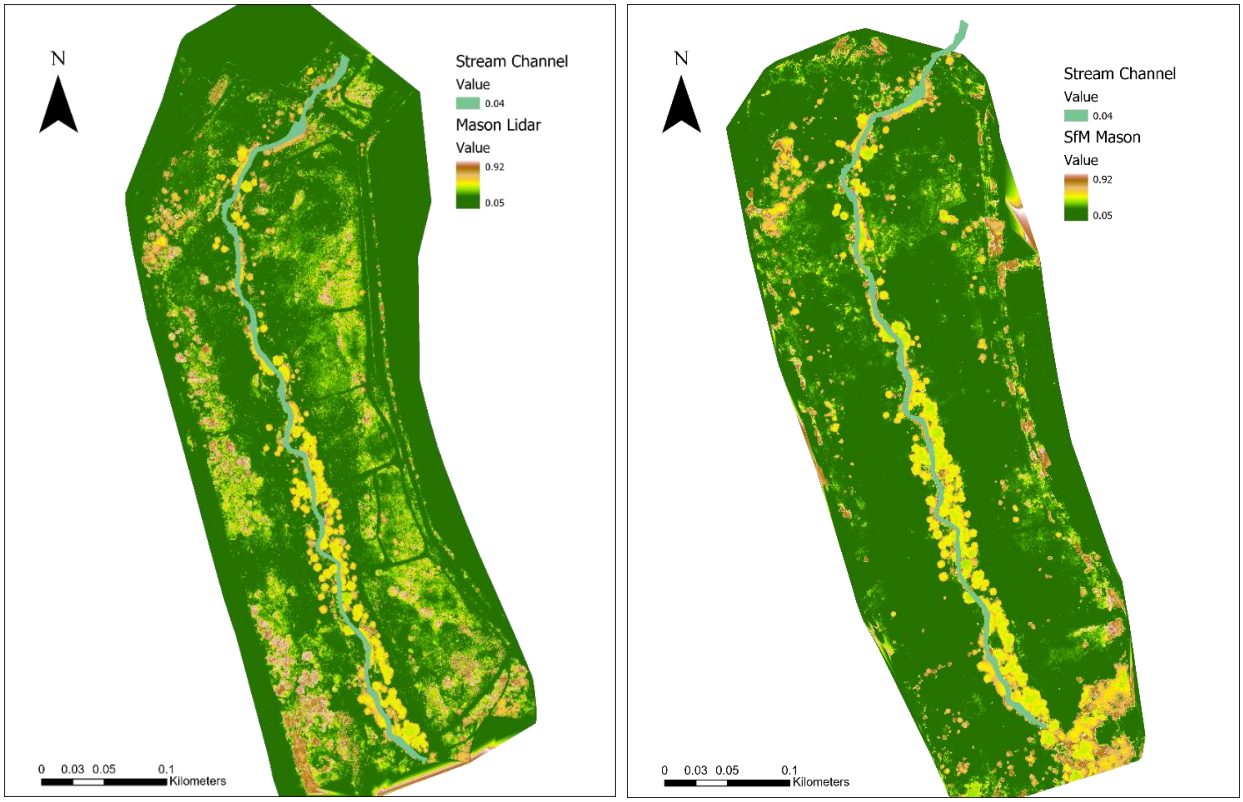

Figure 19. (**a**) The distribution of spatial roughness determined using the DLS Mason method and (**b**) distribution of spatial roughness using the SfM Mason method.

The SfM Mason method (Figure 18b) showed many similarities to the DLS derived raster. However, there was less variability along the fringes of the floodplain furthest from the channel. The lidar (DLS) picked up the low-lying vegetation much better than photogrammetry (SfM). This was especially evident by the appearance of the mowed paths on the eastern side of the study area (Figure 14). This corresponds with the findings of Thomas et al. [61] who found high error (RMSE = ± 1 m) when comparing field and SfM derived grass heights. Visually, the roughness values in the forested riparian area in Figure 16b seemed to be well represented. This is consistent with the findings of Sankey et al. [32], who found strong correlations between SfM

derived and field measured tree height. While they determined the relationship was not as good as DLS tree height (r^2 = 0.9) but was highly correlated (r^2 = 0.7). Another study found a higher correlation between field measured tree height and SfM derived tree height (r^2 = 0.96) but it had a large error value (RMSE = 1.91) [62].

Comparing the statistics between the SfM and DLS Mason models we see a slight increase in the RMSE (Table 7, 8). This means that the high-accuracy DLS data are important, especially for spatially variable roughness estimations. The SfM Mason method outperformed the DLS Chow and Constant *n*, meaning the more spatially variable, calculated roughness is more important than higher quality data.

Because lidar is larger and heavier than most cameras, larger and more expensive drones are needed. Therefore, the costs are much greater (~$150,000) for a lidar unit and large drone, than a smaller drone with a digital camera (~$2,000). Another cost to consider is the sizable processing power to create a dense point cloud using SfM techniques, compared to lidar which computes a raw LAS file with limited processing. The last consideration for SfM is the increased time for the more flights you need for SfM. In this study we needed four photogrammetry flights, which took around 2 hr, to get data comparable to the one 30-min DLS flight to cover the same area. Even with these considerations, SfM is many times less expensive. The difference of 0.01 m RMSE between SfM and DLS data does not justify this increased cost. Further studies are needed to determine if SfM derived DEM data can prove adequate results for 2D hydrodynamic modeling.

2.5 Conclusion

We prepared five hydrodynamic input datasets for the Virginia Tech StREAM Lab to assess the effectiveness of three different vegetative roughness methods and two different data sources. We found a small decrease in RMSE from a more continuous, calibrated roughness derivation method to a more spatially variable calculated method for both SfM and DLS datasets. There was also a decrease in RMSE from SfM derived models to DLS derived models. However, this slight decrease might not justify the increased costs. However additional research is needed to truly compare SfM to DLS since we utilized the DLS derived point cloud to develop the DEM for both simulations. Our research will help inform future 2D hydrodynamic modeling efforts that utilize drone-based remote sensing techniques to develop 2D hydrodynamic models. Our results will help improve hydrodynamic modeling efforts, which are becoming increasingly important for management and planning for the effects of climate change, which has been increasing high-flow events in the Eastern United States.

References

1. Fausch, K.D.; Torgersen, C.E.; Baxter, C. V.; Li, H.W. Landscapes to Riverscapes: Bridging the Gap between Research and Conservation of Stream Fishes. *Bioscience* **2002**, *52*, 483, doi:10.1641/0006-3568(2002)052[0483:ltrbtg]2.0.co;2.
2. Allan, J.D. Landscapes and riverscapes: The influence of land use on stream ecosystems. *Annu. Rev. Ecol. Evol. Syst.* **2004**, *35*, 257–284, doi:10.1146/annurev.ecolsys.35.120202.110122.
3. Tomsett, C.; Leyland, J. Remote sensing of river corridors: A review of current trends and

future directions. *River Res. Appl.* 2019, *35*, 779–803.

4. Groisman, P.Y.; Knight, R.W.; Karl, T.R. Heavy Precipitation and High Streamflow in the Contiguous United States: Trends in the Twentieth Century. *Bull. Am. Meteorol. Soc.* **2001**, *82*, 219–246, doi:10.1175/1520-0477(2001)082<0219:HPAHSI>2.3.CO;2.
5. Hirabayashi, Y.; Mahendran, R.; Koirala, S.; Konoshima, L.; Yamazaki, D.; Watanabe, S.; Kim, H.; Kanae, S. Global flood risk under climate change. *Nat. Clim. Chang.* **2013**, *3*, 816–821, doi:10.1038/nclimate1911.
6. Carbonneau, P.; Fonstad, M.A.; Marcus, W.A.; Dugdale, S.J. Making riverscapes real. *Geomorphology* **2012**, *137*, 74–86, doi:10.1016/j.geomorph.2010.09.030.
7. Kucharczyk, M.; Hugenholtz, C.H.; Zou, X. UAV–LiDAR accuracy in vegetated terrain. *J. Unmanned Veh. Syst.* **2018**, *6*, 212–234, doi:10.1139/juvs-2017-0030.
8. Resop, J.P.; Lehmann, L.; Hession, W.C. Drone Laser Scanning for Modeling Riverscape Topography and Vegetation: Comparison with Traditional Aerial Lidar. *Drones* 2019, *3*, 35.
9. Woodget, A.S.; Austrums, R.; Maddock, I.P.; Habit, E. Drones and digital photogrammetry: from classifications to continuums for monitoring river habitat and hydromorphology. *Wiley Interdiscip. Rev. Water* **2017**, *4*, e1222, doi:10.1002/wat2.1222.
10. Brignoli, L.; Annable, W.K.; Plumb, B.D. Assessing the accuracy of vegetative roughness estimates using unmanned aerial vehicles [UAVs]. *Ecol. Eng.* **2018**, *118*, 73–83, doi:https://doi.org/10.1016/j.ecoleng.2018.01.005.
11. Marteau, B.; Vericat, D.; Gibbins, C.; Batalla, R.J.; Green, D.R. Application of Structure-from-Motion photogrammetry to river restoration. *Earth Surf. Process. Landforms* **2017**, *42*, 503–515, doi:10.1002/esp.4086.

12. Arcement, G.J.; Schneider, V.R. *Guide for selecting Manning's roughness coefficients for natural channels and flood plains*; 1989; Vol. 2339;.

13. Curran, J.C.; Hession, W.C. Vegetative impacts on hydraulics and sediment processes across the fluvial system. *J. Hydrol.* **2013**, *505*, 364–376, doi:10.1016/j.jhydrol.2013.10.013.

14. Manning, R. *On the flow of water in open channels and pipes*; 1891; Vol. 20;.

15. Keys, T.A.; Jones, C.N.; Scott, D.T.; Chuquin, D. A cost-effective image processing approach for analyzing the ecohydrology of river corridors. *Limnol. Oceanogr. Methods* **2016**, *14*, 359–369, doi:10.1002/lom3.10095.

16. Chow, V. *Open-Channel Hydraulics*; McGraw-Hill Book Company, Inc: New York, NY, USA, 1959; ISBN 978-0-07-010776-2.

17. Barnes, H. *Roughness characteristics of natural channels*; USGS Water Supply Paper, 1969; Vol. 7;.

18. Cowan, W.L. Estimating hydraulic roughness coefficients: Agricultural Engineering,. *Agric. Eng.* **1956**, *337*, 470–500.

19. Green, J.C. Modelling flow resistance in vegetated streams: Review and development of new theory. *Hydrol. Process.* **2005**, *19*, 1245–1259, doi:10.1002/hyp.5564.

20. Wang, J.; Zhang, Z. Evaluating Riparian Vegetation Roughness Computation Methods Integrated within HEC-RAS. *J. Hydraul. Eng.* **2019**, *145*, 4019020, doi:10.1061/(ASCE)HY.1943-7900.0001597.

21. Corenblit, D.; Tabacchi, E.; Steiger, J.; Gurnell, A.M. Reciprocal interactions and adjustments between fluvial landforms and vegetation dynamics in river corridors: A review of complementary approaches. *Earth-Science Rev.* **2007**, *84*, 56–86,

doi:https://doi.org/10.1016/j.earscirev.2007.05.004.

22. Abu-Aly, T.R.; Pasternack, G.B.; Wyrick, J.R.; Barker, R.; Massa, D.; Johnson, T. Effects of LiDAR-derived, spatially distributed vegetation roughness on two-dimensional hydraulics in a gravel-cobble river at flows of 0.2 to 20 times bankfull. *Geomorphology* **2014**, *206*, 468–482, doi:10.1016/j.geomorph.2013.10.017.

23. Nepf, H.M. Drag, turbulence, and diffusion in flow through emergent vegetation. *Water Resour. Res.* **1999**, *35*, 479–489, doi:10.1029/1998WR900069.

24. Kouwen, N.; Unny, T.E. Flexible Roughness in Open Channels. *ASCE J Hydraul Div* **1973**, *99*, 713–728.

25. Kouwen, N.N.; Li, R.-M. Biomechanics of vegetative channel linings. *J. Hydraul. Div.* **1980**, *106*.

26. Fathi-Maghadam, M.; Kouwen, N. Nonrigid, nonsubmerged, vegetative roughness on floodplains. *J. Hydraul. Eng.* **1997**, *123*, 51–57, doi:10.1061/(ASCE)0733-9429(1997)123:1(51).

27. Mason, D.C.; Cobby, D.M.; Horritt, M.S.; Bates, P.D. Floodplain friction parameterization in two-dimensional river flood models using vegetation heights derived from airborne scanning laser altimetry. *Hydrol. Process.* **2003**, *17*, 1711–1732, doi:10.1002/hyp.1270.

28. Popescu, S.C.; Wynne, R.H.; Nelson, R.F. Estimating plot-level tree heights with lidar: Local filtering with a canopy-height based variable window size. *Comput. Electron. Agric.* **2003**, *37*, 71–95, doi:10.1016/S0168-1699(02)00121-7.

29. Merwade, V.; Cook, A.; Coonrod, J. GIS techniques for creating river terrain models for hydrodynamic modeling and flood inundation mapping. *Environ. Model. Softw.* **2008**, *23*,

1300–1311, doi:10.1016/j.envsoft.2008.03.005.

30. Straatsma, M.W. Quantitative mapping of hydrodynamic vegetation density of floodplain forests under leaf-off conditions using airborne laser scanning. *Photogramm. Eng. Remote Sensing* **2008**, *74*, 987–998, doi:10.14358/PERS.74.8.987.

31. Tompalski, P.; Coops, N.C.; White, J.C.; Wulder, M.A.; Yuill, A. Characterizing streams and riparian areas with airborne laser scanning data. *Remote Sens. Environ.* **2017**, *192*, 73–86, doi:10.1016/j.rse.2017.01.038.

32. Sankey, T.; Donager, J.; McVay, J.; Sankey, J.B. UAV lidar and hyperspectral fusion for forest monitoring in the southwestern USA. *Remote Sens. Environ.* **2017**, *195*, 30–43, doi:10.1016/j.rse.2017.04.007.

33. Dandois, J.P.; Ellis, E.C. High spatial resolution three-dimensional mapping of vegetation spectral dynamics using computer vision. *Remote Sens. Environ.* **2013**, *136*, 259–276, doi:10.1016/j.rse.2013.04.005.

34. Hugenholtz, C.H.; Whitehead, K.; Brown, O.W.; Barchyn, T.E.; Moorman, B.J.; LeClair, A.; Riddell, K.; Hamilton, T. Geomorphological mapping with a small unmanned aircraft system (sUAS): Feature detection and accuracy assessment of a photogrammetrically-derived digital terrain model. *Geomorphology* **2013**, *194*, 16–24, doi:10.1016/j.geomorph.2013.03.023.

35. Dietrich, J.T. Riverscape mapping with helicopter-based Structure-from-Motion photogrammetry. *Geomorphology* **2016**, *252*, 144–157, doi:10.1016/j.geomorph.2015.05.008.

36. Cruzan, M.B.; Weinstein, B.G.; Grasty, M.R.; Kohrn, B.F.; Hendrickson, E.C.; Arredondo, T.M.; Thompson, P.G. Small Unmanned Aerial Vehicles (Micro-Uavs,

Drones) in Plant Ecology. *Appl. Plant Sci.* **2016**, *4*, 1600041, doi:10.3732/apps.1600041.

37. Rusnák, M.; Sládek, J.; Kidová, A.; Lehotský, M. Template for high-resolution river landscape mapping using UAV technology. *Meas. J. Int. Meas. Confed.* **2018**, *115*, 139–151, doi:10.1016/j.measurement.2017.10.023.

38. Langhammer, J. UAV monitoring of stream restorations. *Hydrology* **2019**, *6*, doi:10.3390/hydrology6020029.

39. Westoby, M.J.; Brasington, J.; Glasser, N.F.; Hambrey, M.J.; Reynolds, J.M. "Structure-from-Motion" photogrammetry: A low-cost, effective tool for geoscience applications. *Geomorphology* **2012**, *179*, 300–314, doi:10.1016/j.geomorph.2012.08.021.

40. Cobby, D.M.; Mason, D.C.; Horritt, M.S.; Bates, P.D. Two-dimensional hydraulic flood modelling using a finite-element mesh decomposed according to vegetation and topographic features derived from airborne scanning laser altimetry. *Hydrol. Process.* **2003**, *17*, 1979–2000, doi:10.1002/hyp.1201.

41. Tamminga, A.; Hugenholtz, C.; Eaton, B.; Lapointe, M. Hyperspatial Remote Sensing of Channel Reach Morphology and Hydraulic Fish Habitat Using an Unmanned Aerial Vehicle (UAV): A First Assessment in the Context of River Research and Management. *River Res. Appl.* **2015**, *31*, 379–391, doi:10.1002/rra.2743.

42. Ballesteros, J.A.; Bodoque, J.M.; Díez-Herrero, A.; Sanchez-Silva, M.; Stoffel, M. Calibration of floodplain roughness and estimation of flood discharge based on tree-ring evidence and hydraulic modelling. *J. Hydrol.* **2011**, *403*, 103–115, doi:10.1016/j.jhydrol.2011.03.045.

43. Schwartz, J. Use of a 2D Hydrodynamic Model for Stream Restoration Design of High-flow Habitat in Low-gradient Midwest Streams. *Prot. Restor. Urban Rural Streams* 2004,

242–251.

44. Cook, A.; Merwade, V. Effect of topographic data, geometric configuration and modeling approach on flood inundation mapping. *J. Hydrol.* **2009**, *377*, 131–142, doi:10.1016/j.jhydrol.2009.08.015.

45. Xiong, Y.F. A dam break analysis using HEC-RAS. *J. Water Resour. Prot.* **2011**, *3*, 370.

46. Violin, C.R.; Cada, P.; Sudduth, E.B.; Hassett, B.A.; Penrose, D.L.; Bernhardt, E.S. Effects of urbanization and urban stream restoration on the physical and biological structure of stream ecosystems. *Ecol. Appl.* **2011**, *21*, 1932–1949.

47. Brunner, G.W. HEC-RAS, River Analysis System Users Manual.

48. Thompson, T.W.; Hession, W.C.; Scott, D. StREAM lab at Virginia tech. *Resour. Eng. Technol. Sustain. World* **2012**, *19*, 8–9, doi:https://doi.org/10.13031/2013.41313.

49. Ries III, K.G.; Newson, J.K.; Smith, M.J.; Guthrie, J.D.; Steeves, P.A.; Haluska, T.L.; Kolb, K.R.; Thompson, R.F.; Santoro, R.D.; Vraga, H.W. *StreamStats, version 4*; Reston, VA, 2017;

50. Benham, B.; Brannan, K.; Dillaha, T.; Mostaghimi, S.; Wagner, R.; Wynn, J.; Yagow, G.; Zeckoski, R. *Benthic TMDL for Stroubles Creek in Montgomery County, Virginia*; Richmond, VA, USA, 2003;

51. Wynn, T.; Hession, W.C.; Yagow, G. *Stroubles Creek Stream Restoration*; Richmond, VA, USA, 2010;

52. Azinheira, D.L.; Scott, D.T.; Hession, W.; Hester, E.T. Comparison of effects of inset floodplains and hyporheic exchange induced by in-stream structures on solute retention. *Water Resour. Res.* **2014**, *50*, 6168–6190, doi:10.1002/2013WR014400.

53. Carbonneau, P.E.; Dietrich, J.T. Cost-effective non-metric photogrammetry from

consumer-grade sUAS: implications for direct georeferencing of structure from motion photogrammetry. *Earth Surf. Process. Landforms* **2017**, *42*, 473–486, doi:10.1002/esp.4012.

54. Fonstad, M.A.; Dietrich, J.T.; Courville, B.C.; Jensen, J.L.; Carbonneau, P.E. Topographic structure from motion: A new development in photogrammetric measurement. *Earth Surf. Process. Landforms* **2013**, *38*, 421–430, doi:10.1002/esp.3366.

55. Kalyanapu, A.J.; Burian, S.J.; McPherson, T.N. Effect of land use-based surface roughness on hydrologic model output. *J. Spat. Hydrol.* **2009**, *9*, 51–71.

56. Hopkinson, C.; Chasmer, L.E.; Sass, G.; Creed, I.F.; Sitar, M.; Kalbfleisch, W.; Treitz, P. Vegetation class dependent errors in lidar ground elevation and canopy height estimates in a boreal wetland environment. *Can. J. Remote Sens.* **2005**, *31*, 191–206, doi:10.5589/m05-007.

57. Kouwen, N. Field estimation of the biomechanical properties of grass. *J. Hydraul. Res.* **1988**, *26*, 559–568, doi:10.1080/00221688809499193.

58. Cobby, D.M.; Mason, D.C.; Horritt, M.S.; Bates, P.D. Two-dimensional hydraulic flood modelling using a finite-element mesh decomposed according to vegetation and topographic features derived from airborne scanning laser altimetry. *Hydrol. Process.* **2003**, *17*, 1979–2000, doi:10.1002/hyp.1201.

59. Watson, D. Hydraulic effects of aquatic weeds in U.K. rivers. *Regul. Rivers Res. Manag.* **1987**, *1*, 211–227, doi:10.1002/rrr.3450010303.

60. Ardıçlıoğlu, M.; Kuriqi, A. Calibration of channel roughness in intermittent rivers using HEC-RAS model: case of Sarimsakli creek, Turkey. *SN Appl. Sci.* **2019**, *1*, 1080, doi:10.1007/s42452-019-1141-9.

61. Thomas, A.F.; Frazier, A.E.; Mathews, A.J.; Cordova, C.E. Impacts of Abrupt Terrain Changes and Grass Cover on Vertical Accuracy of UAS-SfM Derived Elevation Models. *Pap. Appl. Geogr.* **2020**, 1–16, doi:10.1080/23754931.2020.1782254.

62. Isibue, E.W.; Pingel, T.J. Unmanned aerial vehicle based measurement of urban forests. *Urban For. Urban Green.* **2020**, *48*, 126574, doi:https://doi.org/10.1016/j.ufug.2019.126574.

63. Buters, T.M.; Bateman, P.W.; Robinson, T.; Belton, D.; Dixon, K.W.; Cross, A.T. Methodological ambiguity and inconsistency constrain unmanned aerial vehicles as a silver bullet for monitoring ecological restoration. *Remote Sens.* **2019**, *11*, doi:10.3390/rs11101180.

64. Medeiros, S.C.; Hagen, S.C.; Weishampel, J.F. A Random Forest Model Based on Lidar and Field Measurements for Parameterizing Surface Roughness in Coastal Modeling. *IEEE J. Sel. Top. Appl. Earth Obs. Remote Sens.* **2015**, *8*, 1582–1590, doi:10.1109/JSTARS.2015.2419817.

65. US Geological Survey *The National Map—New data delivery homepage, advanced viewer, lidar visualization*; Reston, VA, 2019;

66. van Iersel, W.; Straatsma, M.; Addink, E.; Middelkoop, H. Monitoring height and greenness of non-woody floodplain vegetation with UAV time series. *ISPRS J. Photogramm. Remote Sens.* **2018**, *141*, 112–123, doi:10.1016/j.isprsjprs.2018.04.011.

67. Brasington, J.; Vericat, D.; Rychkov, I. Modeling river bed morphology, roughness, and surface sedimentology using high resolution terrestrial laser scanning. *Water Resour. Res.* **2012**, *48*, doi:10.1029/2012WR012223.

68. Smith, M.W.; Carrivick, J.L.; Hooke, J.; Kirkby, M.J. Reconstructing flash flood

magnitudes using “Structure-from-Motion”: A rapid assessment tool. *J. Hydrol.* **2014**, *519*, 1914–1927, doi:10.1016/j.jhydrol.2014.09.078.

69. Dietrich, J.T. Bathymetric Structure-from-Motion: extracting shallow stream bathymetry from multi-view stereo photogrammetry. *Earth Surf. Process. Landforms* 2017, *42*, 355–364.

70. Woodget, A.S.; Carbonneau, P.E.; Visser, F.; Maddock, I.P. Quantifying submerged fluvial topography using hyperspatial resolution UAS imagery and structure from motion photogrammetry. *Earth Surf. Process. Landforms* **2015**, *40*, 47–64, doi:10.1002/esp.3613.

71. Kinzel, P.J.; Legleiter, C.J.; Nelson, J.M. Mapping River Bathymetry With a Small Footprint Green LiDAR: Applications and Challenges1. *JAWRA J. Am. Water Resour. Assoc.* **2013**, *49*, 183–204, doi:10.1111/jawr.12008.

3. CONCLUSIONS AND FURTHER RESEARCH

3.1 Conclusion

We prepared five hydrodynamic roughness raster data layers for the Virginia Tech StREAM Lab to assess the effectiveness of three different vegetative roughness methods and two different data sources. We found a small decrease in RMSE from a more continuous, calibrated roughness derivation method to a more spatially variable calculated method for both SfM and DLS datasets. There was also a decrease in RMSE from SfM derived models to DLS derived models. However, this slight decrease might not justify the increased costs. However additional research is needed to truly compare SfM to DLS since we utilized the DLS derived point cloud to develop the DEM for both simulations. Our research will help inform future 2D hydrodynamic modeling efforts that utilize drone-based remote sensing techniques to develop 2D hydrodynamic models. Our results will help improve hydrodynamic modeling efforts, which are becoming increasingly important for management and planning for the effects of climate change, which has been increasing high-flow events in the Eastern United States.

3.2 Further Research

In this study we compared high-resolution DLS and SfM photogrammetry techniques for determining Manning's roughness coefficient for use in a 2D hydrodynamic model. While our results provide a useful starting point for future studies and improvements in simulating floods, there are several areas that could use additional exploration, as well as some promising applications that our work suggests might be fruitful.

Additional analyses taking advantage of the flexibility of the Mason method would be valuable. Simply utilizing the stage-dependent roughness capability of the Mason method within a 2D hydrodynamic model would be extremely valuable. In addition, incorporating plant

stiffness values might also improve model simulations. A stiffness value or a drag coefficient could be determined from other remotely sensed data, such as multispectral data [32]. A growing trend of UAV studies is to utilize multiple sensors to assess ecological conditions [63]. For example, Sankey et al. [32] combined DLS with hyperspectral UAV data, found that having both resulted better classification of tree species and detecting forest structure changes. Their study shows the promising potential to fuse lidar and hyperspectral data to classify into plant type. Machine learning could also be utilized to take advantage of the sizeable datasets created by many sources of remote sensed data into useful, classified datasets [63]. Cruzan et al. [36] used k-means classification to determine plant species from SfM derived spectral data and a CHM. Another study used random forest techniques to determine *n* from lidar and other data sources [64], and vegetative metrics, such as stiffness or drag coefficient, could be determined in a similar way.

Like in Mason et al. [27], the k values, or the deflected grass heights, were larger than the canopy height model derived grass heights for both DLS and SfM (Equation 2). Mason theorized that stemmed from slopes used in his study (2×10^{-4}) were lower than in Kouwen and Li [25], who developed the framework for equation 2. However, even with higher slopes in our study area (0.0025), we saw the same issue. To get around this issue, we had to substitute k with the vegetation height h like in Mason [27]. For determining roughness in grassy areas, future studies, different techniques or equations such as those outlined in Wang and Zhang [20] and Corenblit et al. [21].

In our study, we used one DEM (derived from DLS data) consistent for all models in order to focus on the vegetation roughness. For future comparisons of SfM and DLS, there are ways to integrate lidar DEM's into SfM data, such as DEMs developed by the USGS, which may

be adequate for certain reaches [65]. However, ALS derived data are limited in resolution as previously mentioned but are free and do not have restrictions [64]. Further studies will be needed to determine if ALS DEMs, or another data source, can be coupled with UAV SfM photogrammetry data for hydrodynamic modeling purposes.

Compared to DLS, the SfM did not pick up the grass heights well. For future work, utilizing a technique similar to Van Iersal et al. [66] who used normalized digital surface models and linear regression to better determine grass height (RMSE = ± 0.17 - 0.33 m) might be useful. This was an improvement over the findings of Thomas et al. [61], who as referenced in the study reported a 1 m RMSE.

Since we did not focus on low flows, we used constant roughness values within the channel. However, floodplain roughness calculations outlined in this paper could be combined with efforts to calculate in-channel roughness. Brignoli et al. [10] built upon the work of Green [19] to determine the in-channel blockage of aquatic plants using UAV photogrammetry. This method has the potential be adapted to determine floodplain roughness. Other methods used SfM photogrammetry to measure particle grain size [67,68] and standard deviation of elevation [11] to relate to in channel roughness. Methods to determine bathymetry from SfM datasets [69,70] and green-light lidar [71] would lessen the need for time intensive channel surveying, create a more continuous DEM, and likely lead to more accurate simulations. While in channel roughness will not have a significant impact on higher out of channel flood flows, better characterization of in-channel roughness variability would be important for low to moderate (e.g., bankfull flow) simulations with hydrodynamic models.

Appendices

Table 9. Detailed list of data used for this project.

Type	Extent Spatially	Extent Temporally	Measuring Technique
Bridge 2 Stage	1 location	Continuous	Piezometer records WSE
Wells	3 cross sections w/ 6 wells each	Continuous	Piezometer records WSE
Flagged Flood	Throughout floodplain	10/11/2018	Flag locations of flood extent
Velocity Probe	2 locations (channel/floodplain)	June - November, 2019	Velocity Probe Records WSE/Velocity

Table 10. WSE levels determined by model and well data.

Flood	Well	Field Data	Const n	DLS Chow	SfM Chow	DLS Mason	SfM Mason
9/23/2018	1Ad	604.802	604.656	604.657	604.65	604.655	604.658
10/11/2018	1Ad	604.818	604.629	604.631	604.629	604.63	604.632
10/31/2019	1Ad	604.604	604.639	604.636	604.639	604.638	604.639
9/23/2018	1Bd	604.784	604.657	604.619	604.651	604.655	604.659
10/11/2018	1Bd	604.793	604.627	604.632	604.629	604.63	604.633
10/31/2019	1Bd	604.691	604.64	604.637	604.64	604.638	604.64
9/17/2018	1Dd	604.459	604.342	604.339	604.341	604.329	604.33
9/23/2018	1Dd	604.749	604.63	604.63	604.622	604.615	604.618
9/28/2018	1Dd	604.574	604.448	604.451	604.453	604.439	604.435
10/20/2019	1Dd	604.447	604.396	604.396	604.398	604.388	604.384
9/23/2018	1Ed	604.762	604.616	604.616	604.609	604.609	604.539

10/11/2018	1Ed	604.713	604.587	604.588	604.586	604.584	604.496
10/31/2019	1Ed	604.637	604.598	604.593	604.597	604.592	604.508
9/23/2018	2Cd	604.6328	604.494	604.492	604.485	604.458	604.46
10/11/2018	2Cd	604.6471	604.468	604.467	604.465	604.434	604.434
9/17/2018	2Dd	604.2187	604.221	604.218	604.22	604.198	604.208
9/23/2018	2Dd	604.4864	604.493	604.492	604.485	604.457	604.462
9/28/2018	2Dd	604.3331	604.323	604.326	604.328	604.254	604.307
10/11/2018	2Dd	604.4745	604.467	604.467	604.465	604.433	604.436
9/23/2018	2Ed	604.576	604.494	604.492	604.485	604.455	604.46
9/28/2018	2Ed	604.416	604.324	604.325	604.327	604.301	604.305
10/11/2018	2Ed	604.571	604.464	604.467	604.464	604.432	604.435
10/20/2019	2Ed	604.246	604.274	604.274	604.276	604.254	604.261
10/27/2019	2Ed	604.139	604.185	604.186	604.187	604.169	604.18
10/31/2019	2Ed	604.456	604.465	604.472	604.475	604.439	604.441
9/23/2018	3Bd	604.119	604.256	604.252	604.246	604.183	604.192
9/28/2018	3Bd	603.952	604.085	604.086	604.089	604.073	604.074
10/11/2018	3Bd	604.082	604.231	604.228	604.226	604.163	604.171
10/31/2019	3Bd	604.18	604.241	604.233	604.236	604.169	604.176
9/23/2018	3Cd	604.152	604.259	604.256	604.249	604.189	604.187
9/28/2018	3Cd	603.982	604.098	604.099	604.101	604.042	604.059
10/11/2018	3Cd	604.145	604.235	604.232	604.23	604.166	604.165
10/20/2019	3Cd	603.863	604.05	604.049	604.051	603.996	604.02
10/31/2019	3Cd	604.127	604.245	604.237	604.24	604.173	604.171
9/17/2018	3Dd	603.812	603.991	603.989	603.989	603.932	603.962
9/23/2018	3Dd	604.132	604.256	604.253	604.245	604.185	604.178
9/28/2018	3Dd	603.949	604.092	604.094	604.095	604.036	604.05
10/11/2018	3Dd	604.128	604.231	604.228	604.225	604.162	604.156
10/20/2019	3Dd	603.812	604.044	604.044	604.044	603.989	604.012
10/27/2019	3Dd	603.678	603.96	603.958	603.958	603.902	603.936
9/17/2018	3Ed	603.823	603.977	603.974	603.976	603.922	603.953
9/23/2018	3Ed	604.142	604.245	604.241	604.234	604.171	604.167

9/28/2018	3Ed	603.966	604.08	604.08	604.082	604.024	604.039
10/11/2018	3Ed	604.143	604.22	604.216	604.214	604.147	604.144
10/20/2019	3Ed	603.806	604.031	604.03	604.032	603.979	604.002
10/27/2019	3Ed	603.583	603.945	603.942	603.944	603.891	603.926
10/31/2019	3Ed	603.981	604.23	604.221	604.224	604.155	604.15
9/23/2018	3Fd	604.154	604.238	604.233	604.227	604.162	604.158
9/28/2018	3Fd	604.1	604.072	604.073	604.076	604.019	604.032
10/11/2018	3Fd	604.284	604.212	604.209	604.207	604.139	604.136
10/31/2019	3Fd	603.842	604.222	604.214	604.217	604.146	604.141

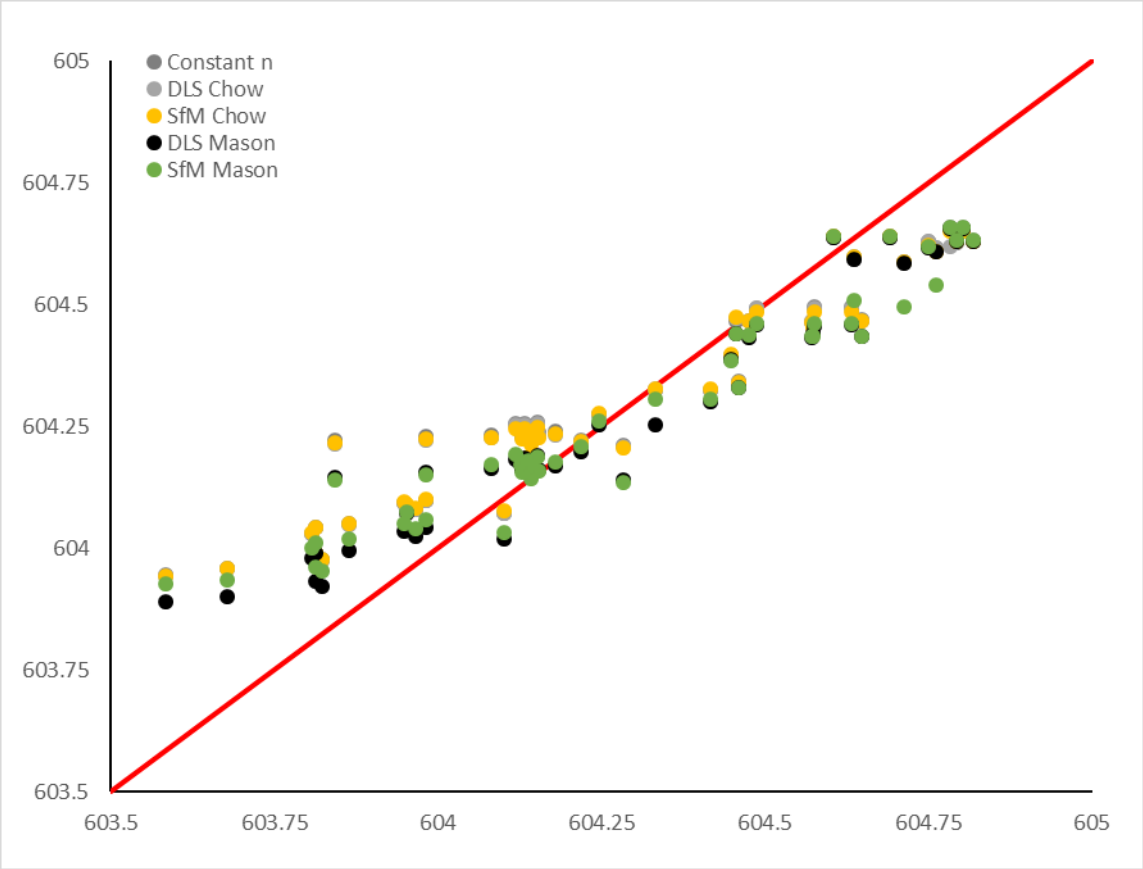

Figure 20. Comparing all models with Well WSE data.

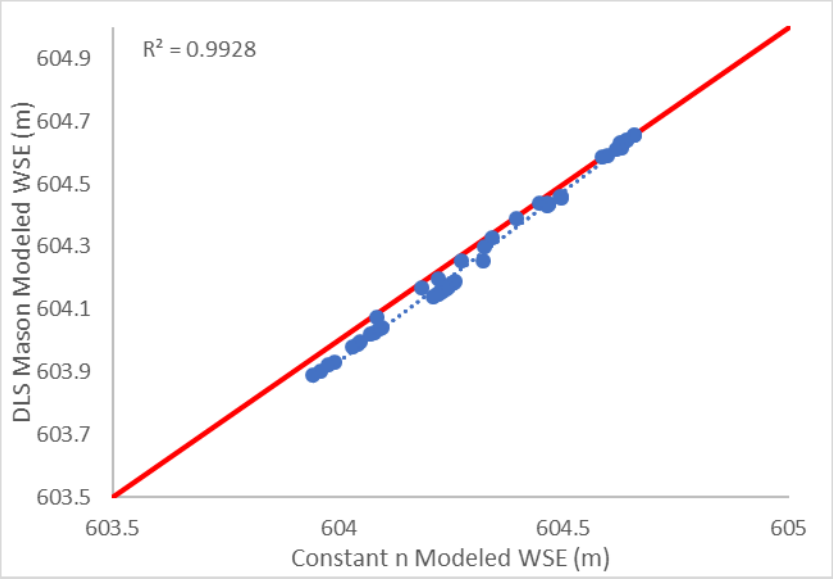

Figure 21. Comparing DLS Mason to Constant n WSE models.